Modelling of viscoelastic properties and crack growth in bituminous mixtures: Application to the simulation of crack growth in semi-circular samples subjected to oxidative ageing

Akoêtê Bernus Kouevidjin, Jean-François Barthélémy, Saannibe Ciryle Somé, Hachmi Ben Dhia, Virginie Mouillet

Modelling of viscoelastic properties and crack growth in bituminous mixtures: Application to the simulation of crack growth in semi-circular samples subjected to oxidative ageing.

B. Kouevidjin[1,2], J.-F. Barthélémy[1], C. Somé[1], H. Ben Dhia[2], and V. Mouillet[3]

[1]Cerema, Univ. Gustave Eiffel, UMR MCD, F-77171 Sourdun, France
[2]Paris-Saclay University, CentraleSupelec, MSSMat Laboratory, 91191 Gif-sur-Yvette
[3]Cerema, Univ. Gustave Eiffel, UMR MCD, F-13100 Aix-en-Provence, France

Abstract

This paper presents the development of a mechanical crack propagation model coupling viscoelasticity and the extended Griffith's criterion to the dissipative medium. The applications are related to the study of mode I cracking of bituminous materials subjected to loading rates under intermediate temperature condition and long term ageing duration. The viscoelastic behaviour of these materials based on a Generalized Maxwell (GM) model is presented and a discretized form of the state equation based on the exponential algorithm is given. The simulation of the complex modulus test is used to validate the proposed discretized law. Then, the thermodynamic framework of the Griffith criterion extended to the GM's model is revisited. A crack growth criterion is derived involving the viscoelastic energy release rate ($\mathcal{G}_\vartheta$) as a thermodynamic driving force capped by a resistance strength ($\mathcal{R}$-curve). Analytical and numerical implementations of the $\mathcal{G}_\vartheta$ on a semi-circular bending geometry (SCB) are presented. SCB fracture tests following a standard experimental protocol are then simulated. The resistance strength parameters taking into account the fracture process zone effect are identified by an optimisation technique resulting in a good agreement between the test results and the numerical simulations. This study demonstrates that the proposed approach can account for the ductile fracture properties of bituminous mixes.

keywords: bituminous mixes, ageing, viscoelasticity, crack growth

1 Introduction

Cracking represents one of the main risk of pavement damage over the time. It is often accelerated by the ageing of bitumen in bituminous pavement. Understanding of the effect of ageing on the mechanical and fracture properties of bituminous mixes is therefore a key step in predicting the service life of pavement structures. Most of the studies in the literature deals with the effect of ageing on rheological properties of binders and mixes [1–3]. These studies agree that the stiffness modulus increases with ageing. However, the effect of ageing on the cracking resistance of bituminous mixes is still under investigation. Only Brah's et al. and Farhad et al. works [4–6] combine these two aspects by limiting their investigations either to one loading rate or to a single test temperature. At low temperatures, their studies show that the fracture parameters are even more degraded as the ageing time increases. At these temperatures, bituminous mixes are often considered as brittle or quasi-brittle elastic materials and under the assumption of a negligible fracture process zone around the crack tip, several works have been conducted applying linear elastic fracture mechanics (LEFM) to study the fracture behaviour of bituminous mixes [7–12]. Generally, the size of the fracture process zone is relatively large in these materials which limits the accuracy of the predictive models based on the LEFM concepts.

The crack growth mechanism in bituminous mixes is relatively complex and involves the use of fracture mechanics principles combined with time and temperature dependent constitutive models to accurately capture crack initiation and growth. The high complexity inherent in modelling bituminous mixes as a heterogeneous material leads to the assumption of an isotropic viscoelastic homogeneous material in most modelling approaches. Relatively few studies deal with the modelling of fracture in viscoelastic materials.

The first works on fracture mechanics based approaches in this domain include the important contributions of Knauss [13, 14] and Schapery [15–17]. From the extended viscoelastic correspondence principle [18], R. A. Schapery [17] proposed a viscoelastic integral $\mathcal{J}_\vartheta$ extending Rice's integral, used in linear elastic fracture mechanics, to viscoelastic materials. Based on this theory, several time-dependent cracking models taking into account viscous deformations have been proposed (e.g. [19, 20]). The application of this technique of calculation of the energy release rate is very limited, as the conditions of application of the extended correspondence principle do not lend itself to all real problems. Dubois et al. [21–25] developed a new method of invariant surface integral $\mathcal{G}\theta_v$ to compute the rate of energy restitution. Based on Brincker's description [26], Dubois et al. introduced two intensity factors, namely the viscoelastic opening

intensity factor to determine the relative displacements in the vicinity of the crack bottom and the stress intensity factor, already known in LEFM. They proposed an alternative formulation of the $\mathcal{G}\theta_v$ integral calculation using the spectral decomposition of the reduced viscoelastic compliance: starting from a generalized Kelvin-Voigt rheological model (KVG) of n Kelvin-Voigt branches, these authors decoupled the general cracking problem into n elastic sub-problems by assuming that the total displacement can be decomposed into a sum of elastic displacement of each Kelvin-Voigt chain. This presents a concern due to the fact that the strain fields in the Kelvin-Voigt chains are generally not geometrically compatible.

Cohesive zone models (CZMs) are the most widely used numerical local damage models for modelling crack initiation and growth in bituminous mixes [27–35]. The different tensile-separation laws of the CZM models are discussed in [36]. Li and Marasteanu [28], Kim and Buttlar [33] investigated the fracture behaviour of asphalt mixtures under low temperature conditions using the CZM bilinear law. Song et al.[30] and Arago et al.[35] modeled the crack growth in bituminous mixes at room temperature by considering the exponential and bilinear approaches of the time-independent cohesive model associated with the viscoelastic behaviour of the material, respectively. While the CZM model is widely used in the bituminous mixes community, it is still subject to debate. Indeed, although the method is academically interesting, one can naturally question the fact that the viscoelastic behaviour of the material is locally disturbed by an elastic law. To overcome this problem, C. Yoon et al. [37] recently proposed a non-linear viscoelastic cohesive zone (NVCZ) model with a damage function making the model dependent on this. Kim et al. [38] applied the NVCZ model to study a bituminous media fracture by considering a Gaussian law as damage function. Their studies revealed that the proposed model takes into account the rate-dependent effect and can successfully predict test results at different rates by only taking the results at an arbitrary loading rate. One of the drawbacks of this model is that it introduces additional parameters whose determination is not that easy. In addition, these models may suffer a mesh dependence.

Non-local damage models are another technique for simulating material crack initiation and growth. Several authors have recently extended some of these models to viscoelastic media: the phase field approach [39–42], the Thick Level Set model [43]. The latest has been applied, in 1D case, to model the uniaxial tensile stress tests of bituminous mixes at differents temperatures.

In this paper, we focus on the modelling of crack propagation by using Griffith's macroscopic viewpoint [44].

Nguyen et al. [45] modeled crack propagation in a viscoelastic medium. In their work, the ther-

modynamic framework of viscoelastic crack propagation was revisited using the Burger model. They showed that this approach allows to highlight the loading rate effect on the behaviour of the crack growth driving force and the evolution of the crack length. They also investigated the interaction between viscous dissipation and fracture growth in geological materials subjected to long-term loading [46]. Relying on rigorous thermodynamic basis, this efficient approach could be used to study crack growth in bituminous mixes. However, the used rheological model does not allow to describe the thermomechanical behaviour of bituminous mixes over a wide range of solicitation's frequencies.

In this study, this energetic approach is extended to the Generalized Maxwell model, in order to predict the fracture behaviour of bituminous mixtures.

To this end, this paper is organized as follows.

Section 2 presents the materials and the ageing protocol of the loose mixtures. Section 3 describes test methods for the characterisation of viscoelastic (complex modulus test) and cracking (semi-circular bending test) properties of bituminous mixtures. In section 4, in the perspective of numerical developments of boundary value problems, an explicit incremental form of the viscoelastic behaviour law is presented. The thermodynamic framework of crack propagation in viscoelastic media is then revisited. A crack growth criterion taking into account the viscous effects is derived. The energy release rate, representing the crack growth driving force, is identified in a form that allows its numerical determination in the framework of the previous incremental approach. The section 5 discusses the proposed energy release rate expressions for the case of a semi-circular geometry subjected to 3-point bending. The numerical implementation of this quantity is then illustrated by confronting the numerical results with the proposed expressions and by examining the nature of the asymptotic responses of this driving force. In addition, the stability of crack growth in dissipative media is discussed. It reveals the role played by the resistance to fracture, i.e. the critical energy release rate. Finally, a validation of the proposed crack growth criterion is presented in section 6. The selected form of the critical energy release rate is discussed and different comparisons between simulations and experimental results are carried out.

2 Materials and mix design

2.1 Materials properties

The mixes are produced with a paving grade bitumen 35/50, whose properties of needle penetration (EN 1426) [47] and softening temperature (EN 1427) [48] are respectively 42 × 0.1 mm and 53.2 °C, and porphyry aggregates which come from *Pont de Colonne* (in France) quarry whose abrasion loss and fragmentation properties respectively known as Microdeval (EN 1097-1) [49] value and Los Angeles (EN 1097-2) [50] value are 17% and 8%. It is used for surface and binder courses and labelled AC10 mix. The mixture composition and the densities of the constituents are given in Table 1.

Constituent	Volume fraction (in %)	Density (in $kg.m^{-3}$)
Limestone filler	2.8	2700
0/2	26.1	
2/6.3	23.7	2630
6.3/10	42.	
Bitumen	5.4	1040

Table 1: Composition of mixture AC10

2.2 Ageing of bituminous mixture

The ageing protocol adopted in the curent study is the RILEM ageing procedure described in [51]. The mixes are manufactured at 165°C. After the mixing, the loose mixture are cooled down to 135°C and spread in thin layer (not more than 2.5 cm) into a tray and placed in a ventilated oven. Part of the mixture is kept at this temperature for 8 hours to simulate a short term ageing. Then, they are cooled down to 85°C and kept respectively in the oven for 3 and 6 days to reproduce the long term ageing. 2 hours before the end of the ageing procedure, the loose mixes are reheated at 165°C and then compacted. The reference mix is compacted without long-term ageing and designated V0 while those subject to 8 hours short-term ageing followed by long-term ageing are labeled V3, V6 for respectively 3 and 6 days ageing.

3 Test methods

3.1 Complex modulus test: 2-point cantilever beam method

At the end of the ageing process, the loose mixes are compacted according to EN 12697-33 [52]. The manufactured bituminous slabs are then sawn into prismatic specimens of dimensions 4 ×

4 × 12 cm and subjected to complex modulus measurements. Sinusoidal cyclic deflections are performed on a prismatic cantilever beam in accordance to EN 12697-26 (Annex A: 2PB-PR [53]). During the test, thermal conditioning of the specimens is ensured by a thermal chamber. A temperature probe located near the surface of the specimen is used to measure the temperature. Fig. 1 shows a general view of the experiment. Tests are performed at 4 frequencies (from 3 Hz

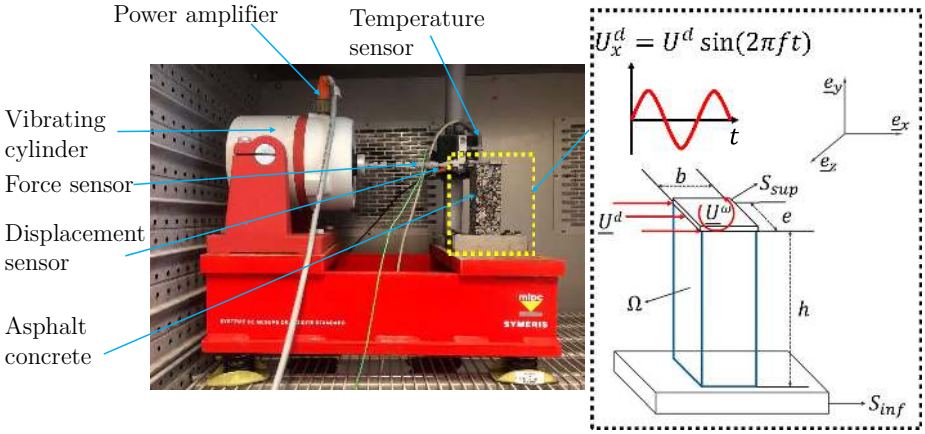

Fig. 1. Mixes complex modulus $E^*(\omega)$ test principle: b= 40 mm , e= 40 mm , h= 120 mm

to 40 Hz) and at 8 temperatures (from -30 to 50°C). The measured force F and the imposed displacement U allow to calculate the complex modulus $|E^*|$ according to a calculation provided in [53]. The isotherms of $|E^*|$ are then used to build the master curves (see Fig. 2). Complex modulus test results are modeled using the Generalized Maxwell (GM) model [54]. The GM analytical expression of the complex Youngs modulus is given by the following equation (1):

$$E^*(\omega) = E_0 + \sum_{i=1}^{i=m} \left(\frac{E_i j\omega\tau_i}{1 + j\omega\tau_i} \right) \tag{1}$$

Where E_i and τ_i respectively represent the i^{th} spring modulus and characteristic time. E_i and τ_i are determined at each isotherm by minimizing the error between $E^*_{measured}$ and E^*_{GM} according to the least-squares method (see Fig. 2). The fitted parameters corresponding to each aged mixes are given in Table 2 at reference temperature T_{ref}=20°C.

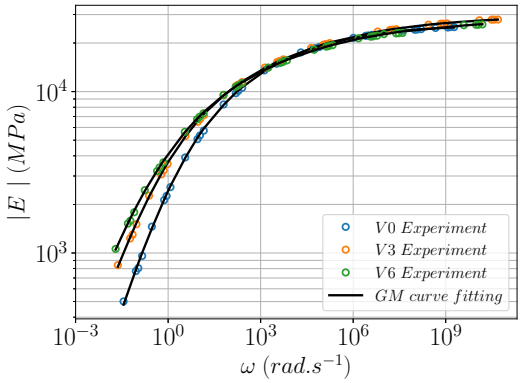

Fig. 2. Master curve of complex modulus of AC10 at T_{ref}=20.°C

3.2 Crack growth in semi-circular bituminous mix specimen: experiment

3.2.1 Specimen preparation

The test specimens have been manufactured in laboratory and gyratory compacted. The obtained cylindrical samples have been sliced to obtain 50 mm thick cylinders with 150 mm in diameter then cut to obtain semi-circular specimens as schematized in Fig. 3. The specimens have been selected in such that their void contents are close to (7±0.6)%. At least four specimens have been used.

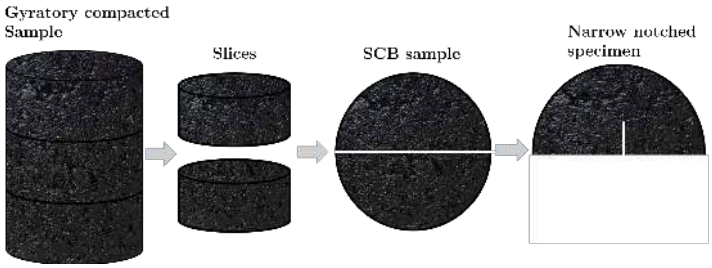

Fig. 3. SCB specimen's preparation

3.2.2 Experimental test procedure

The loading system consists of a three-point bending loading cell placed in UTICELL Type 650 mechanical testing equipment. Before the test, the specimens are placed in a thermo-regulated chamber for 24 hours to reach temperature equilibrium before testing. They have been taken out of the chamber and placed in the loading cell rapidly to perform the test in less than a minute. The loading cell consists of two rigid roller supports and lateral thick metallic plates

which allows placing the specimen onto the bending fixture in order to avoid exentric loading. Another roller support allows applying the load vertically. The test principle is represented in Fig. 4. Lubrication is applied to the supports to mitigate friction during testing. The specimens

Fig. 4. SCB test device

diameters are D=150 mm, resulting in a span length of 120 mm between two cylindrical support of 25 mm. The specimen thickness is t=50 mm. The notch length and width are respectively $\ell = 10$ mm and $w_\ell = 0.35$ mm. Monotonic displacement rate is applied on the specimen until failure. The force, the time and the vertical load-line displacement are recorded continuously during the test by sensors integrated into the loading system. The tests are performed at 20°C and a loading rate of 1 mm.min^{-1} and 5 mm.min^{-1} for the reference hot mix V0 and for the aged mixes V3 and V6. Figure Fig. 5 shows typical force-displacement curves for an AC10 at 1 mm.min^{-1} and 5 mm.min^{-1}.

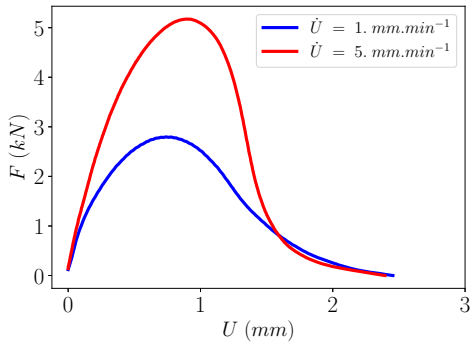

Fig. 5. Typical test results of AC10 at 20°C for two loading rate

4 Modelling of viscoelastic crack growth in SCB

4.1 Problem formulation

Let us consider the process of crack growth in opening mode in a notched two-dimensional viscoelastic body Ω subjected to prescribed displacement $\underline{U}^d(t)$ and force $\underline{T}^d(t)$ respectively on Γ_u and Γ_T (see Fig. 6). We assume that the crack does not appear on the edge part of $\Gamma_u \cup \Gamma_T$ where either a displacement is prescribed or a force is non-zero. For the sake of simplicity, body forces and inertia effects are neglected and the small perturbation's hypotheses are considered.

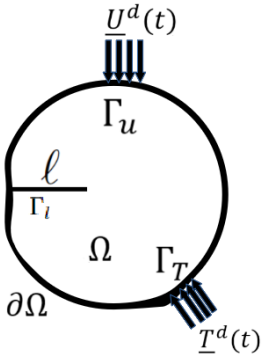

Fig. 6. Cracked viscoelastic domain

Based on these assumptions, the mechanical problem $(\mathcal{P})$ can be formulated as follows.

$$(\mathcal{P}): \begin{cases} \mathrm{div}\underline{\underline{\boldsymbol{\sigma}}}(\underline{x},t) = \underline{0} & \text{in } \Omega \\ \underline{u}(\underline{x},t) = \underline{U}^d(t) & \text{on } \Gamma_u \\ \underline{\underline{\boldsymbol{\sigma}}}(\underline{x},t).\underline{n} = \underline{T}^d(t) & \text{on } \Gamma_T \\ \underline{\underline{\boldsymbol{\sigma}}}(t) = \mathcal{R}_t\left[\begin{smallmatrix}\tau=t\\ \underline{\underline{\boldsymbol{\varepsilon}}}(\tau)\\ \tau=-\infty\end{smallmatrix}\right] & \text{in } \Omega \\ \underline{\underline{\boldsymbol{\varepsilon}}}(\underline{u}) = \frac{1}{2}\left(\underline{\underline{\nabla}}\,\underline{u} + {}^T\underline{\underline{\nabla}}\,\underline{u}\right) & \text{in } \Omega \end{cases} \tag{2}$$

where $\mathcal{R}_t[]$ is termed *the modulus functional* [55], which maps the entire history strain to the stress value at the current time t. The Neumann-type boundary conditions in equation (2) indirectly assume that the stress vector is zero on the rest of the domain edge including the pre-crack.

The linear viscoelastic behaviour has historically been described by rheological models combining

springs and linear dampers, some of which provide an expression for the mathematical functional $\mathcal{R}_t[]$.

In most cases, instead of invoking boundary condition fields as $\underline{U}^d(t)$ and $\underline{T}^d(t)$, the loading mode may be described by a set of prescribed static parameters $(Q_1^d(t)\cdots Q_p^d(t))$ associated to kinematic variables $(q_1(t)\cdots q_p(t))$ and prescribed kinematic parameters $(q_{p+1}^d(t)\cdots q_n^d(t))$ associated to static variables $(Q_{p+1}(t)\cdots Q_n(t))$ (see [56]). The whole set of loading parameters is thus given by a vector $\underline{\mathscr{C}}(t) = \left[Q_1^d(t),\cdots,Q_p^d(t),q_{p+1}^d(t),\cdots,q_n^d(t)\right]^T$ and the associated static and kinematic variables are defined by duality such that the power of external forces writes:

$$\begin{aligned} P_e &= \underline{Q}\cdot\dot{q} \\ &= \sum_{i=1}^{p} Q_i^d\,\dot{q}_i + \sum_{i=p+1}^{n} Q_i\,\dot{q}_i^d, \end{aligned} \tag{3}$$

where the whole static vector defining external forces contains both prescribed and resulting components $\underline{Q}(t) = \left[Q_1^d(t),\cdots,Q_p^d(t),Q_{p+1}(t),\cdots,Q_n(t)\right]^T$ and so is, by duality, the kinematic vector $q(t) = \left[q_1(t),\cdots,q_p(t),q_{p+1}^d(t),\cdots,q_n^d(t)\right]^T$.

4.2 Viscoelastic constitutive law for bituminous mixes

In this study, we chose to use the Generalized Maxwell (GM) model [54] to model the behaviour of bituminous mixtures in the time domain. It should be noted that the Huet [57] model and the 2S2P1D model [58] describe very well the bituminous mixtures behaviour. However, these models lead to store the loading history from the initial to the current time, which may be very costly in a finite element approach. As recalled in the sequel, the GM type of model is well adapted to an incremental formulation of the behaviour allowing to calculate a stress state at a given time step from the strain and stress states at the previous time. It is also interesting to note that the constitutive laws of bituminous mixtures under variable temperature have been proposed using Huet's [59] and generalized Maxwell's [41].

4.2.1 3D non-ageing isotropic linear viscoelastic formulation

The constitutive law of bituminous mixtures based on the GM model shown in Fig. 7 is given by the Stieltjes convolution integral below [55]:

$$\underline{\underline{\boldsymbol{\sigma}}}(t) = \int_{t_0}^{t} \underset{\sim}{\boldsymbol{R}}\left(t-t'\right) : \mathrm{d}\underline{\underline{\boldsymbol{\varepsilon}}}(t'), \tag{4}$$

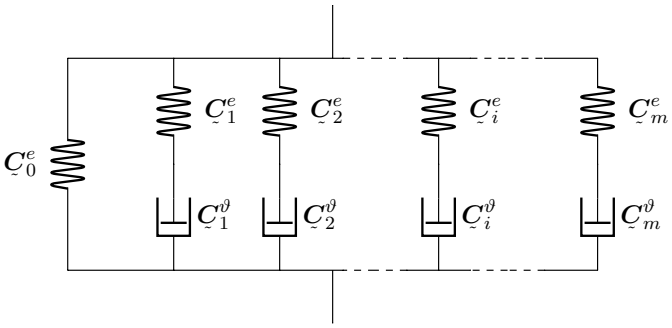

Fig. 7. Generalized Maxwell model (GM)

where

$$\underset{\sim}{\boldsymbol{R}}(t) = \underset{\sim}{\boldsymbol{C}}_0 + \sum_{i=1}^{m} \exp\left(-\frac{t}{\tau_i}\right)\underset{\sim}{\boldsymbol{C}}_i. \tag{5}$$

In the case of a constant Poisson's ratio (which will be the case in this paper unless otherwise stated), the relaxation tensor can be written in the following form:

$$\underset{\sim}{\boldsymbol{R}}(t) = \overline{R}(t)\underset{\sim}{\boldsymbol{C}}^{el} \tag{6}$$

with :

$$\begin{aligned} \overline{R}(t) &= \frac{R(t)}{E^{el}}, \text{ where } R(t) = \left(E_0 + \sum_{i=1}^{m} E_i \exp\left(-\frac{t}{\tau_i}\right)\right) \quad \text{and } E^{el} = \sum_{i=0}^{m} E_i \\ \underset{\sim}{\boldsymbol{C}}^{el} &= \frac{E^{el}}{1-2\nu}\underset{\sim}{\boldsymbol{J}} + \frac{E^{el}}{1+\nu}\underset{\sim}{\boldsymbol{K}} \end{aligned} \tag{7}$$

where $\boldsymbol{J}_{ijkl} = \frac{1}{3}\delta_{ij}\delta_{kl}$ stands for the volumetric part components of the fourth-order unity tensor $\boldsymbol{I}$ ($\boldsymbol{I}_{ijkl} = \frac{1}{2}(\delta_{ik}\delta_{jl} + \delta_{il}\delta_{jk})$), $\boldsymbol{K} = \boldsymbol{I} - \boldsymbol{J}$ denotes the deviatoric part of $\boldsymbol{I}$, $\overline{R}$ and E^{el} are respectively the normalized relaxation function and the instantaneous elastic modulus and E_i the Young's modulus of the ith spring in the GM model.

4.2.2 Incremental formulation

Solving the viscoelastic problem formulated above (equation (4)) by the usual quadrature methods is less efficient and often leads to numerical instabilities. Indeed, these methods are stable only if the computational time step is very small ($dt << \tau_i$), requiring several computational steps in the case of very slow phenomena simulations. In order to overcome this problem, an

unconditionally stable algorithm, called exponential algorithm, developed by Z. P. Bazant [60], V. Šmilauer and Z. P. Bažant [61] is used. The physical time interval $T = [t_0, T_{max}]$ is discretized into a sequence of intervals $\Delta_n t$ such that: $t_{n+1} = t_n + \Delta_n t$, T_{max} being the maximum simulation time. By rewriting equation (4) at time step t_{n+1}, exploiting the properties of the exponential function; splitting the time integral into two, one from t_0 to t_n where the solution is known and the other from t_n to t_{n+1} where the solution is unknown; and approximating the time derivative of the total strain tensor over the time interval $[t_n; t_{n+1}]$ by the following finite difference:

$$\frac{\mathrm{d}\underline{\underline{\boldsymbol{\varepsilon}}}}{\mathrm{d}t'}(t') \simeq \frac{\underline{\underline{\boldsymbol{\varepsilon}}}(t_{n+1}) - \underline{\underline{\boldsymbol{\varepsilon}}}(t_n)}{\Delta_n t} \qquad \forall\, t' \in [t_n, t_{n+1}]; \tag{8}$$

it can be shown that equation (4) leads to an affine relationship between the total stress and total strain tensors:

$$\Delta_n \underline{\underline{\boldsymbol{\sigma}}} = \underset{\sim}{\boldsymbol{C}}(\Delta_n t) : \Delta_n \underline{\underline{\boldsymbol{\varepsilon}}} + \underline{\underline{\widetilde{\boldsymbol{\sigma}}}}(t_n) \tag{9}$$

where

$$\underset{\sim}{\boldsymbol{C}}(\Delta_n t) \;=\; \underset{\sim}{\boldsymbol{C}}_0 + \sum_{i=1}^{m} \frac{\tau_i}{\Delta_n t}\left(1 - \exp\left(-\frac{\Delta_n t}{\tau_i}\right)\right)\underset{\sim}{\boldsymbol{C}}_i, \tag{10a}$$

$$\underline{\underline{\widetilde{\boldsymbol{\sigma}}}}(t_n) \;=\; \sum_{i=1}^{m}\left(\exp\left(-\frac{\Delta_n t}{\tau_i}\right) - 1\right)\underline{\underline{\boldsymbol{\sigma}}}_i(t_n), \tag{10b}$$

$$\underline{\underline{\boldsymbol{\sigma}}}_i(t_{n+1}) \;=\; \exp\left(-\frac{\Delta_n t}{\tau_i}\right)\underline{\underline{\boldsymbol{\sigma}}}_i(t_n) + \frac{\tau_i}{\Delta_n t}\left(1 - \exp\left(-\frac{\Delta_n t}{\tau_i}\right)\right)\underset{\sim}{\boldsymbol{C}}_i : \Delta_n \underline{\underline{\boldsymbol{\varepsilon}}} \tag{10c}$$

The formula (9) appears as a pseudo-elastic law with pre-stress where only the current and previously calculated fields are involved. The pre-stress $\underline{\underline{\widetilde{\boldsymbol{\sigma}}}}(t_n)$ accounts for all past stress history updated and stored at the end of each time increment.

Considering a non-ageing isotropic linear viscoelastic behaviour, in which case the fourth-order tensor $\underset{\sim}{\boldsymbol{C}}$ can be completely defined by two scalar viscoelastic kernels $\lambda(t)$ and $\mu(t)$ [55], formula (9) can be expressed as follows:

$$\Delta_n \underline{\underline{\boldsymbol{\sigma}}} = \lambda(\Delta_n t)\mathrm{tr}(\Delta_n \underline{\underline{\boldsymbol{\varepsilon}}})\underline{\underline{\boldsymbol{I}}} + 2\mu(\Delta_n t)\Delta_n \underline{\underline{\boldsymbol{\varepsilon}}} + \underline{\underline{\widetilde{\boldsymbol{\sigma}}}}(t_n), \tag{11}$$

where:

$$\lambda(\Delta_n t) = \lambda_0 + \sum_{i=1}^{m} \frac{\tau_i}{\Delta_n t}\left(1 - \exp\left(-\frac{\Delta_n t}{\tau_i}\right)\right)\lambda_i, \tag{12a}$$

$$\mu(\Delta_n t) = \mu_0 + \sum_{i=1}^{m} \frac{\tau_i}{\Delta_n t}\left(1 - \exp\left(-\frac{\Delta_n t}{\tau_i}\right)\right)\mu_i, \tag{12b}$$

In the case of a constant Poisson' s ratio, the equations (12a) and (12b) reduce to:

$$\lambda(\Delta_n t) = \frac{\nu E^{el}}{(1+\nu)(1-2\nu)}\overline{R}^*(\Delta_n t) \tag{13a}$$

$$\mu(\Delta_n t) = \frac{E^{el}}{2(1+\nu)}\overline{R}^*(\Delta_n t) \tag{13b}$$

with:

$$\overline{R}^*(t) = \frac{R^*(t)}{E^{el}}, \text{ where } R^*(t) = \left(E_0 + \sum_{i=1}^{m} \frac{\tau_i}{t}\left(1 - \exp\left(-\frac{t}{\tau_i}\right)\right)E_i\right) \tag{14}$$

The incremental constitutive law given by equation (11) can be introduced in a finite element discretization to obtain solutions to complex viscoelastic problems, as will be discussed in sections 4.2.3 and 4.3.

4.2.3 3D modelling of the 2-point loads cantilever beam test

For FE modelling, the tested asphalt concrete AC10 is supposed to be homogeneous and isotropic, which is a common assumption. In addition, recent work by A. Gudmarsson et al. [62] and F. Allou et al. [63] on the measurement of the complex Poisson's ratio of bituminous mixes showed very low values of its imaginary part compared to its real part. The complexity of the measurement and the dispersion of the obtained results are additional factors to be considered. For these reasons, it is considered that the Poisson's ratio is constant at 0.35 (a value often used in structural calculations). For clarity, only the reference material V0 is chosen for the modelling and its properties are given in Table 2. The geometry and boundary conditions are presented in Fig. 1.

The mechanical problem, at each time increment, is then governed by the following system of

Table 2: Fitted GM model parameters at $20°C$

V0		V3		V6	
$E_i\ (MPa)$	$\tau_i\ (s)$	$E_i\ (MPa)$	$\tau_i\ (s)$	$E_i\ (MPa)$	$\tau_i\ (s)$
2.20×10^3	4.13×10^{-9}	2.41×10^3	4.12×10^{-10}	2.58×10^3	1.69×10^{-10}
2.49×10^3	5.16×10^{-7}	1.12×10^3	7.64×10^{-9}	1.57×10^3	9.27×10^{-9}
3.04×10^3	1.33×10^{-5}	2.57×10^3	1.34×10^{-7}	1.68×10^3	1.82×10^{-7}
2.99×10^3	1.65×10^{-4}	2.58×10^3	2.85×10^{-6}	9.39×10^2	1.38×10^{-6}
2.93×10^3	1.33×10^{-3}	7.22×10^2	8.01×10^{-5}	1.65×10^3	6.47×10^{-6}
1.88×10^3	6.35×10^{-3}	2.36×10^3	2.13×10^{-5}	2.02×10^3	5.35×10^{-5}
2.26×10^3	2.29×10^{-2}	2.98×10^3	2.82×10^{-4}	8.35×10^2	2.64×10^{-4}
3.74×10^2	2.34×10^{-2}	$3,48 \times 10^3$	2.72×10^{-3}	1.42×10^3	5.32×10^{-4}
2.74×10^3	1.39×10^{-1}	1.17×10^3	1.38×10^{-2}	1.37×10^3	1.89×10^{-3}
1.57×10^2	5.77×10^{-1}	$1,41 \times 10^3$	3.00×10^{-2}	1.56×10^3	5.34×10^{-3}
3.81×10^2	6.02×10^{-1}	1.29×10^3	4.73×10^{-2}	2.20×10^3	1.99×10^{-2}
1.19×10^3	9.35×10^{-1}	2.49×10^3	2.33×10^{-1}	2.57×10^3	1.09×10^{-1}
6.67×10^2	3.03×10^0	1.76×10^3	1.17×10^0	2.19×10^3	6.96×10^{-1}
5.54×10^2	1.19×10^1	1.40×10^3	8.03×10^0	1.44×10^3	4.48×10^0
2.48×10^2	8.21×10^1	1.67×10^2	7.67×10^1	8.17×10^2	2.86×10^1
1.07×10^2	–	3.37×10^2	7.76×10^1	2.38×10^2	1.48×10^2
		1.42×10^2	–	3.11×10^2	2.57×10^2
				2.09×10^2	–

equations:

$$
\left(\mathcal{P}^{n+1}\right)_s : \left\{
\begin{array}{lcl}
\mathrm{div}\underline{\underline{\boldsymbol{\sigma}}}(\underline{x}, t_{n+1}) & = & \underline{0} \quad \text{in} \quad \Omega \\
\underline{u}(\underline{x}, t_{n+1}) & = & \left\{ \begin{array}{ll} \underline{U}^d(\underline{x}, t_{n+1}) + \underline{U}^\omega(\underline{x}, t_{n+1}) & \text{on} \quad S_{sup} \\ \underline{0} & \text{on} \quad S_{inf} \end{array} \right. \\
\underline{U}^d(\underline{x}, t_{n+1}) & = & U^d \sin\left(2\pi f t_{n+1}\right) \underline{e}_x \\
\underline{U}^\omega(\underline{x}, t_{n+1}) & = & \underline{\omega} \wedge \underline{GM} \quad \text{where} \quad \left\{ \begin{array}{lcl} \underline{\omega}(t_{n+1}) & = & \omega(t_{n+1}) \underline{e}_z \\ \underline{GM} & = & \left(x - \dfrac{b}{2}\right) \underline{e}_x + \left(z - \dfrac{b}{2}\right) \underline{e}_z \end{array} \right. \\
\underline{\underline{\boldsymbol{\sigma}}}(\underline{x}, t_{n+1}).\underline{n} & = & \underline{0} \quad \text{on} \quad \partial\Omega \setminus \{S_{sup} \cup S_{inf}\} \\
\underline{\underline{\boldsymbol{\sigma}}}(\underline{x}, t_{n+1}) & = & \underline{\underline{\boldsymbol{\sigma}}}(\underline{x}, t_n) + \lambda(\Delta_n t)\mathrm{tr}(\Delta_n \underline{\underline{\boldsymbol{\varepsilon}}}(\underline{x}))\underline{\underline{\boldsymbol{I}}} \quad \text{in} \quad \Omega \\
 & & +2\mu(\Delta_n t)\Delta_n \underline{\underline{\boldsymbol{\varepsilon}}}(\underline{x}) + \underline{\underline{\widetilde{\boldsymbol{\sigma}}}}(\underline{x}, t_n) \\
\underline{\underline{\boldsymbol{\varepsilon}}}(\underline{u}(\underline{x}, t_{n+1})) & = & \dfrac{1}{2}\left(\nabla \underline{u}(\underline{x}, t_{n+1}) + {}^T\nabla \underline{u}(\underline{x}, t_{n+1})\right) \quad \text{in} \quad \Omega
\end{array}
\right. \tag{15}
$$

where the amplitude of the imposed displacement cycle U^d and the frequency f are input data

while the rotation ω is an additional unknown of the problem to solve. The unknown variable ω is a simple scalar that is not related to a finite element description insofar as it does not refer to a degree of freedom attached to any single node. Indeed, it accounts for the fact that the upper surface of the sample undergoes a rigid body motion and its value has to be adjusted so that the overall bending moment around $\underline{e}_z$ acting over the upper surface cancels out.

Note that the kinematic boundary condition on S_{sup} in its general form is written: $\underline{u}(\underline{x}, t_{n+1}) = \underline{U}^d(\underline{x}, t_{n+1}) + \underline{\omega} \wedge \underline{GM}$ where the components of the displacement vector of the center of the plate $\underline{U}^d$ and the rotation vector $\underline{\omega}$ define either prescribed parameters of the problem or Lagrange multipliers associated to their corresponding dual static parameters (force or moment components). Here, for symmetry reasons, it is anticipated that both $\underline{U}^d.\underline{e}_z = 0$ and $\underline{R}.\underline{e}_z = 0$ ($\underline{R}$ is the resultant reaction on S_{sup}) as well as both $\underline{\omega}.\underline{e}_x = 0$ and $\underline{\mathcal{M}}.\underline{e}_x = 0$ ($\underline{\mathcal{M}}$ is the resultant moment vector at the center G of S_{sup}) so that prescribed kinematic parameters ($\underline{U}^d.\underline{e}_z = 0$ and $\underline{\omega}.\underline{e}_x = 0$) are preferably considered in the problem. In addition, since the loading system is screwed to the plate by applying a sinusoidal translation along x (thus $\underline{U}^d.\underline{e}_x = U^d \sin(2\pi f t_{n+1})$ and $\underline{R}.\underline{e}_y = 0$), the plate prevents a torsional rotation, thus $\underline{\omega}.\underline{e}_y = 0$. Finally, instead of imposing a null vertical force $\underline{R}.\underline{e}_y = 0$, it is assumed by analogy with the study of a pure bending problem in classical structure mechanics that $\underline{U}^d.\underline{e}_y = 0$ (null elongation of the neutral axis in absence of normal force) and we therefore obtain the kinematic boundary condition on S_{sup} given in equation (15). Finally, as mentioned above, the only (unknown) kinematic Lagrange multiplier is $\omega = \underline{\omega}.\underline{e}_z$ associated with a prescribed null moment around $\underline{e}_z$.

In the sequel, we adopt the following notation: $g(\underline{x}, t_n) = g^n$ for any volume or surface field g. For the approximation of $\left(\mathcal{P}_s^{n+1}\right)$ by means of the finite element method (e.g. [64]), the weak formulation of this problem is needed. It is given by:

Find the quadruplet $(\underline{u}^{n+1}, \underline{p}^{n+1}, \underline{q}^{n+1}, \omega^{n+1})$ in $\mathcal{U} \times \mathcal{U}^{'}(S_{inf}) \times \mathcal{U}^{'}(S_{sup}) \times \mathbb{R}$:

$$
\begin{cases}
\displaystyle\int_\Omega \left[\lambda(\Delta_n t)\mathrm{tr}(\underline{\underline{\varepsilon}}^{n+1})\underline{\underline{\boldsymbol{I}}} + 2\mu(\Delta_n t)\underline{\underline{\varepsilon}}^{n+1}\right] : \underline{\underline{\varepsilon}}(\delta\underline{u})\,\mathrm{d}\Omega - \int_{S_{inf}} \underline{p}^{n+1}\cdot\delta\underline{u}\,\mathrm{d}S - \int_{S_{sup}} \underline{q}^{n+1}\cdot\delta\underline{u}\,\mathrm{d}S = \\
\displaystyle\int_\Omega \left[\lambda(\Delta_n t)\mathrm{tr}(\underline{\underline{\varepsilon}}^{n})\underline{\underline{\boldsymbol{I}}} + 2\mu(\Delta_n t)\underline{\underline{\varepsilon}}^{n} - \underline{\underline{\boldsymbol{\sigma}}}^{n} - \underline{\underline{\widetilde{\boldsymbol{\sigma}}}}^{n}\right] : \underline{\underline{\varepsilon}}(\delta\underline{u})\,\mathrm{d}\Omega \qquad \forall\,\delta\underline{u} \in \mathcal{U} \\
\displaystyle\int_{S_{inf}} \underline{u}^{n+1}\cdot\delta\underline{p}\,\mathrm{d}S = 0 \qquad \forall\,\delta\underline{p} \in \mathcal{U}^{'}(S_{inf}) \\
\displaystyle\int_{S_{sup}} \left(\underline{u}^{n+1} - \underline{\omega}^{n+1}\wedge\underline{GM}\right)\cdot\delta\underline{q}\,\mathrm{d}S = \int_{S_{sup}} \underline{U}^{d,n+1}\delta\underline{q}\,\mathrm{d}S \qquad \forall\,\delta\underline{q} \in \mathcal{U}^{'}(S_{sup}) \\
\displaystyle\int_{S_{sup}} \left(\underline{GM}\wedge\underline{q}^{n+1}\right)\cdot\underline{e}_z\delta\omega\,\mathrm{d}S = 0 \qquad \forall\,\delta\omega \in \mathbb{R}
\end{cases}
\tag{16}
$$

where $\mathcal{U}$ denotes the set of admissible displacement fields (set of smooth continuous displacement fields on Ω), $\mathcal{U}^{'}(S_{inf})$ (respectively $\mathcal{U}^{'}(S_{sup})$) is the set of admissible forces (Lagrange multipliers space) on S_{inf} (respectively S_{sup}) defined by duality with respect to $\mathcal{U}$, i.e. such that the integrals on S_{sup} (respectively S_{sup}) in (16) are defined for any kinematic field belonging to $\mathcal{U}$.

The Lagrangian corresponding to (16) is as follows:

$$
\begin{aligned}
&\mathcal{L}(\underline{u}^{n+1}, \underline{p}^{n+1}, \underline{q}^{n+1}, \omega^{n+1}) = \frac{1}{2}\int_\Omega \underline{\underline{\varepsilon}}(\underline{u}^{n+1}) : \left((3\lambda(\Delta_n t) + 2\mu(\Delta_n t))\underset{\sim}{\boldsymbol{J}} + 2\mu(\Delta_n t)\underset{\sim}{\boldsymbol{K}}\right) : \underline{\underline{\varepsilon}}(\underline{u}^{n+1})\,\mathrm{d}\Omega + \\
&\int_\Omega \left[\underline{\underline{\boldsymbol{\sigma}}}^{n} + \underline{\underline{\widetilde{\boldsymbol{\sigma}}}}^{n} - \lambda(\Delta_n t)\mathrm{tr}(\underline{\underline{\varepsilon}}^{n})\underline{\underline{\boldsymbol{I}}} - 2\mu(\Delta_n t)\underline{\underline{\varepsilon}}^{n}\right] : \underline{\underline{\varepsilon}}(\underline{u}^{n+1})\,\mathrm{d}\Omega - \int_{S_{inf}} \underline{p}^{n+1}\cdot\underline{u}^{n+1}\,\mathrm{d}S - \\
&\int_{S_{sup}} \underline{q}^{n+1}\cdot\left(\underline{u}^{n+1} - \underline{U}^{d,n+1} - \underline{\omega}^{n+1}\wedge\underline{GM}\right)\,\mathrm{d}S
\end{aligned}
\tag{17}
$$

The incremental viscoelastic problem equation (16) is implemented in a generic finite element library GetFEM [65]. The resolution algorithm is described by the flowchart in Fig. 8. Fig. 9a to Fig. 9d compare the numerical results with the experimental results of force versus displacement values at a temperature of 20°C and for four loading frequencies (from 3Hz to 30Hz). A fairly good agreement between these results can be observed. This validates the implemented incremental method.

The developed program is used in the following section to model the crack propagation during the SCB test.

4.3 Crack growth modelling in a viscoelastic medium: Energetic approach

When the cracking and loading states are known, the problem $(\mathcal{P})$ can be solved using the approach presented above. All that remains is to define a crack growth criterion. For this purpose, the energetic approach to model mode I crack propagation in a two-dimensional viscoelastic medium adapted from the work of S. T. Nguyen et al. [68] is presented.

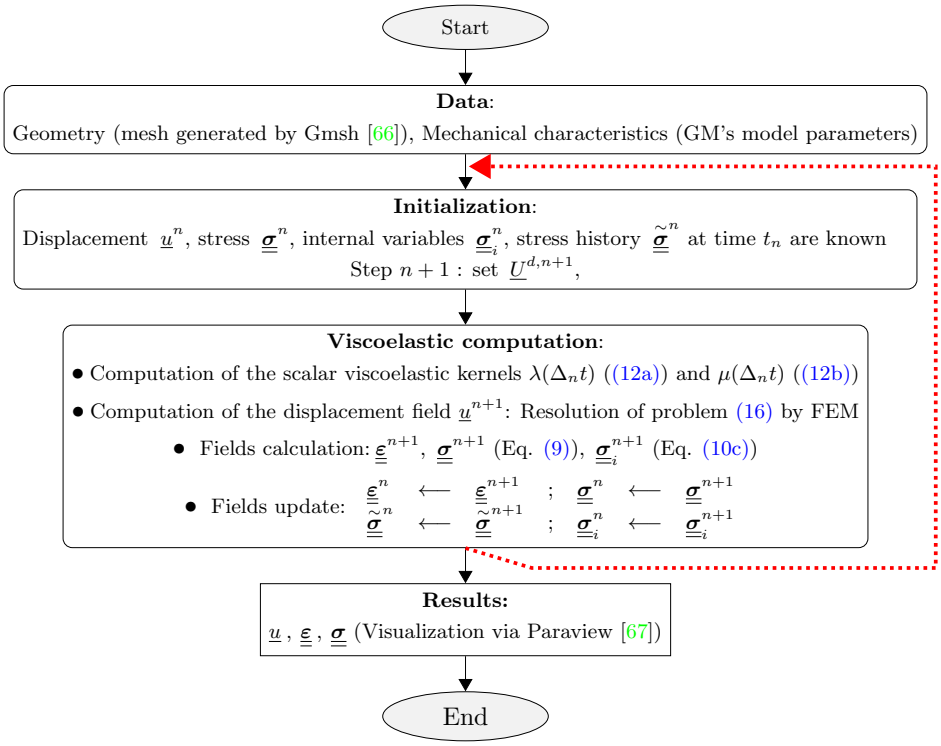

Fig. 8. Flowchart of the program implemented in GetFEM

4.3.1 Thermodynamic analysis

The developments of this section are much inspired by [68]. In the case of an isothermal and uniform transformation, the first two principles of thermodynamics lead a dissipation given by:

$$\mathcal{D} = P_e - \dot{\mathcal{W}} \geq 0 \tag{18}$$

where $\mathcal{W}$ denotes the elastic strain energy stored in the system and P_e the power of external forces. For a finer analysis of the inequality (18), an alternative formulation of the state equation (4) is proposed as follows:

$$\underline{\underline{\boldsymbol{\sigma}}}(t) = \underset{\sim}{\boldsymbol{C}}^{el} : \left(\underline{\underline{\boldsymbol{\varepsilon}}} - \underline{\underline{\boldsymbol{\varepsilon}}}^{\vartheta}\right) \tag{19}$$

where:

$$\underline{\underline{\boldsymbol{\varepsilon}}}^{\vartheta}(t) \;=\; \underset{\sim}{\boldsymbol{C}}^{el^{-1}} : \sum_{i=1}^{m} \underset{\sim}{\boldsymbol{C}}_i : \underline{\underline{\boldsymbol{\varepsilon}}}_i^{\vartheta}(t) \tag{20}$$

$\underline{\underline{\boldsymbol{\varepsilon}}}_i^{\vartheta}$ represents the viscous strain in the i^{th} Maxwell element and $\underline{\underline{\boldsymbol{\varepsilon}}}^{\vartheta}$ can be interpreted as an eigenstrain tensor.

In order to analyze more in details the dissipation (18), it is worth observing first that the elastic strain energy is a function of the loading parameters, which have been synthesized by the vector $\underline{\mathscr{E}}(t) =$

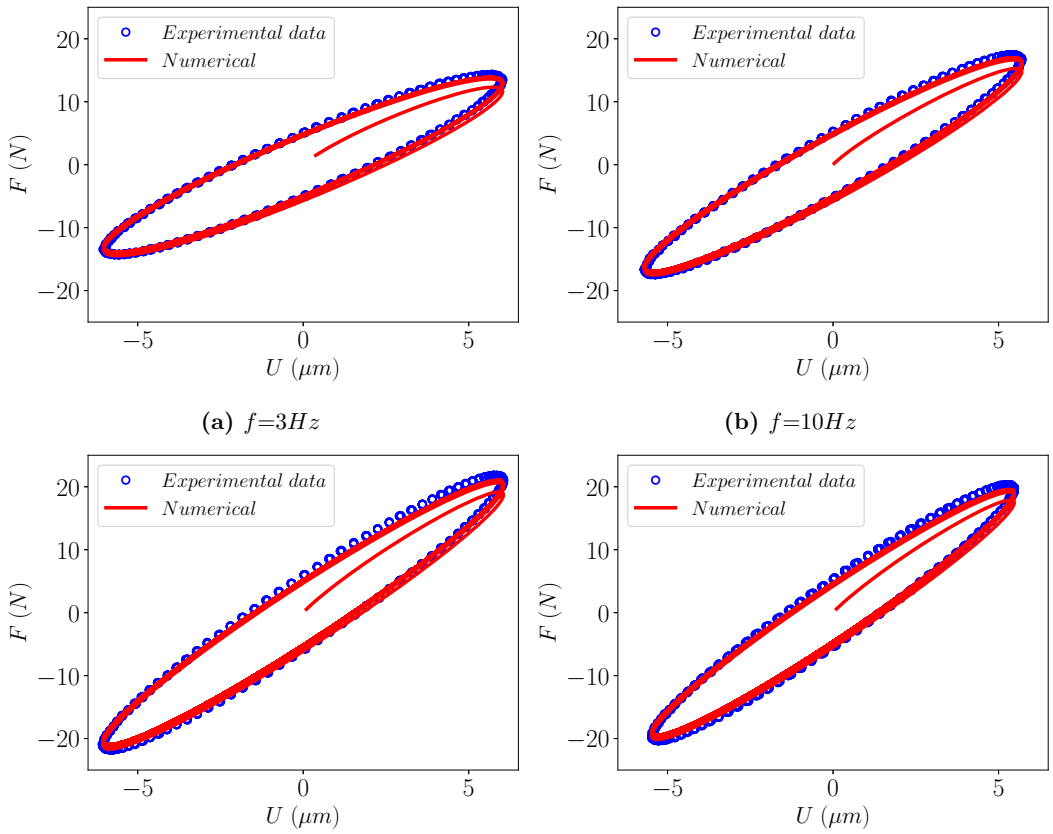

(a) f=3Hz **(b)** f=10Hz

(c) f=25Hz **(d)** f=30Hz

Fig. 9. Simulation of the 2-points cantilever beam test: Evolution of numerical and experimental forces versus the imposed displacement at 20°C

$\left[Q_1^d(t), \cdots, Q_p^d(t), q_{p+1}^d(t), \cdots, q_n^d(t)\right]^T$, of the crack length $\ell(t)$ as well as the internal variables fields $\{\underline{\underline{\boldsymbol{\varepsilon}}}_i^{\vartheta}(t)\ ,\ i = 1, m\}$ and writes:

$$\mathcal{W}(\underline{\mathscr{C}}, \ell, \{\underline{\underline{\boldsymbol{\varepsilon}}}_i^{\vartheta}\}) = \frac{1}{2}\int_{\Omega}\left[\underline{\underline{\boldsymbol{\varepsilon}}} : \underset{\sim}{\boldsymbol{C}}_0 : \underline{\underline{\boldsymbol{\varepsilon}}} + \sum_{i=1}^{m}\left(\underline{\underline{\boldsymbol{\varepsilon}}} - \underline{\underline{\boldsymbol{\varepsilon}}}_i^{\vartheta}\right) : \underset{\sim}{\boldsymbol{C}}_i : \left(\underline{\underline{\boldsymbol{\varepsilon}}} - \underline{\underline{\boldsymbol{\varepsilon}}}_i^{\vartheta}\right)\right] \mathrm{d}\Omega \tag{21}$$

Besides, the power of external forces has been expressed in (3) and it is clear that any evolution leaving ℓ and the internal fields $\underline{\underline{\boldsymbol{\varepsilon}}}_i^{\vartheta}$ unchanged while allowing changes of the loading parameters $\underline{\mathscr{C}}$ corresponds to an elastic evolution which does not induce any dissipation by definition:

$$\left.\frac{\partial \mathcal{W}}{\partial \mathscr{C}_i}\right|_{(\ell, \{\underline{\underline{\boldsymbol{\varepsilon}}}_i^{\vartheta}\})} \dot{\mathscr{C}}_i = \underline{Q} \cdot \left.\frac{\partial \underline{q}}{\partial \mathscr{C}_i}\right|_{(\ell, \{\underline{\underline{\boldsymbol{\varepsilon}}}_i^{\vartheta}\})} \dot{\mathscr{C}}_i \tag{22}$$

It follows that the remaining terms of the dissipation stem only from the evolutions of ℓ and $\underline{\underline{\boldsymbol{\varepsilon}}}_i^{\vartheta}$:

$$\mathcal{D} = -\frac{\partial}{\partial \ell}\left(\mathcal{W}-\phi\right)\Big|_{(\underline{\mathscr{C}},\{\underline{\underline{\boldsymbol{\varepsilon}}}_i^{\vartheta}\})}\dot{\ell} - \frac{\partial}{\partial\{\underline{\underline{\boldsymbol{\varepsilon}}}_i^{\vartheta}\}}\left(\mathcal{W}-\phi\right)\Big|_{(\underline{\mathscr{C}},\ell)} \bullet \{\dot{\underline{\underline{\boldsymbol{\varepsilon}}}}_i^{\vartheta}\} \tag{23}$$

where $\bullet$ denotes a scalar product in the sense of functions (i.e. written under the form of integrals since $\underline{\underline{\boldsymbol{\varepsilon}}}_i^{\vartheta}$ are actual fields) and ϕ is the work of given external forces written as:

$$\phi = \sum_{i=1}^{p} Q_i^d\, q_i, \tag{24}$$

Note that ϕ in (24) does not include terms corresponding to given kinematic parameters since the latter disappear in the power of external forces for evolutions of $\underline{q}$ at fixed $\underline{\mathscr{C}}$.

Then, by designating by $P = \mathcal{W} - \phi$ the potential energy and by denoting:

$$\mathcal{D}_{\vartheta} = -\left.\frac{\partial P}{\partial\{\underline{\underline{\boldsymbol{\varepsilon}}}_i^{\vartheta}\}}\right|_{(\underline{\mathscr{C}},\ell)} \bullet \{\dot{\underline{\underline{\boldsymbol{\varepsilon}}}}_i^{\vartheta}\}, \tag{25}$$

the energy dissipated by the crack growth appears to be the complementary of the viscous term in the total dissipation:

$$\mathcal{D} - \mathcal{D}_{\vartheta} = -\left.\frac{\partial P}{\partial \ell}\right|_{(\underline{\mathscr{C}},\{\underline{\underline{\boldsymbol{\varepsilon}}}_i^{\vartheta}\})}\dot{\ell}, \tag{26}$$

where $\mathcal{G}_{\vartheta} = -\left.\dfrac{\partial P}{\partial \ell}\right|_{(\underline{\mathscr{C}},\{\underline{\underline{\boldsymbol{\varepsilon}}}_i^{\vartheta}\})}$ represents the thermodynamic force associated with the crack growth.

The specificity of this energy release rate relies on the fact that its value depends on the viscous strain field which, in turn, depends on the loading history $\underline{\mathscr{C}}(t)$ and the evolution of the crack length $\ell(t)$ over the considered time interval.

By following the assumption formulated in the work of S. T. Nguyen et al. [68] that the dissipation related to crack growth is proportional to the propagation rate $\dot{\ell}$, we have:

$$\mathcal{D} - \mathcal{D}_{\vartheta} = \mathcal{R}\dot{\ell} \tag{27}$$

where $\mathcal{R}$ can be interpreted as a resistance strength that must be overcome for crack growth to occur. By merging equations (26) and (27), the crack growth criterion can be formulated as follows:

$$\begin{cases} \mathcal{G}_{\vartheta} < \mathcal{R} \implies \dot{\ell} = 0 & \text{(no crack growth)} \\ \mathcal{G}_{\vartheta} = \mathcal{R} \implies \dot{\ell} \geq 0 & \text{(possible crack growth)} \end{cases} \tag{28}$$

The main difficulty in the study of cracking in dissipative media lies in the determination of these two terms and will be discussed in the next section.

4.3.2 Energy released rate computation

The energy release rate expression $\mathcal{G}_\vartheta$ highlights a partial derivative with respect to the crack length ℓ of the potential energy. This partial derivative is approximated, from two crack states ℓ and $\ell + \delta\ell$, by a difference between the potential energies calculated for these two states. This is a small elastic variation related to an increase $\delta\ell$ of the crack length since the derivation is performed by blocking the viscous strains and the imposed loading. To demonstrate this, let us consider the alternative formulation of the behaviour law equation (19) for the real state of cracking corresponding to length ℓ:

$$\underline{\underline{\boldsymbol{\sigma}}}(\ell) = \underset{\sim}{\boldsymbol{C}}^{el} : \underline{\underline{\boldsymbol{\varepsilon}}}(\ell) + \underline{\underline{\boldsymbol{\sigma}}}^r(\ell) \tag{29}$$

where:

$$\underline{\underline{\boldsymbol{\sigma}}}^r(\ell) = -\underset{\sim}{\boldsymbol{C}}^{el} : \underline{\underline{\boldsymbol{\varepsilon}}}^\vartheta(\ell)$$

The auxiliary elementary calculation for the fictitious cracking state $l + \delta l$ is instead governed by the following state equation:

$$\underline{\underline{\boldsymbol{\sigma}}}(\ell + \delta\ell) = \underset{\sim}{\boldsymbol{C}}^{el} : \underline{\underline{\boldsymbol{\varepsilon}}}(\ell + \delta\ell) + \underline{\underline{\boldsymbol{\sigma}}}^r(\ell) \tag{30}$$

By combining equations (29) and (30), the variation in stress between these two cracking states is thus given by equation (31):

$$\Delta_\ell \underline{\underline{\boldsymbol{\sigma}}} = \underset{\sim}{\boldsymbol{C}}^{el} : \Delta_\ell \underline{\underline{\boldsymbol{\varepsilon}}}, \tag{31}$$

which represents the instantaneous response of viscoelastic behaviour. The approximated expression for the energy release rate is given by:

$$\begin{aligned} \mathcal{G}_\vartheta &= -\frac{\delta P}{\delta \ell} \\ &= -\frac{(\mathcal{W} - \phi)(\ell + \delta\ell) - (\mathcal{W} - \phi)(\ell)}{\delta\ell} \end{aligned} \tag{32}$$

In summary, the energy release rate at time t characterised by the cracking state ℓ is calculated in two steps:

Step (1): Solving the problem $(\mathcal{P})$ with the viscoelastic behaviour law and deriving $\mathcal{W}(\ell)$ by the equation (33) and the work of given external forces by (34).

$$\mathcal{W}(\ell) = \frac{1}{2} \int_\Omega \left[\underline{\underline{\boldsymbol{\varepsilon}}}(\ell) : \underset{\sim}{\boldsymbol{C}}_0 : \underline{\underline{\boldsymbol{\varepsilon}}}(\ell) + \sum_{i=1}^{m} \left(\underline{\underline{\boldsymbol{\varepsilon}}}(\ell) - \underline{\underline{\boldsymbol{\varepsilon}}}_i^\vartheta(\ell) \right) : \underset{\sim}{\boldsymbol{C}}_i : \left(\underline{\underline{\boldsymbol{\varepsilon}}}(\ell) - \underline{\underline{\boldsymbol{\varepsilon}}}_i^\vartheta(\ell) \right) \right] \mathrm{d}\Omega \tag{33}$$

$$\phi(\ell) = \sum_{i=1}^{p} Q_i^d \, q_i(\ell) \tag{34}$$

where $\underline{q}(\ell)$ is the kinematic parameter resulting from solving the problem $(\mathcal{P})$.

Step (2): Solving an auxiliary elastic problem characterised by the cracking state $\ell + \delta\ell$ subjected to the

same loading with the behaviour law (31) (where the viscous strain fields are those calculated in step (1)) and deriving $\mathcal{W}(\ell+\delta\ell)$ by the equation (35) and the work of given external forces by (36).

$$\mathcal{W}(\ell+\delta\ell) = \frac{1}{2}\int_\Omega \left[\underline{\underline{\varepsilon}}(\ell+\delta\ell) : \underset{\sim}{\boldsymbol{C}}_0 : \underline{\underline{\varepsilon}}(\ell+\delta\ell) + \sum_{i=1}^{m} \left(\underline{\underline{\varepsilon}}(\ell+\delta\ell) - \underline{\underline{\varepsilon}}_i^{\vartheta}(\ell)\right) : \underset{\sim}{\boldsymbol{C}}_i : \left(\underline{\underline{\varepsilon}}(\ell+\delta\ell) - \underline{\underline{\varepsilon}}_i^{\vartheta}(\ell)\right) \right] \mathrm{d}\Omega \tag{35}$$

$$\phi(\ell+\delta\ell) = \sum_{i=1}^{p} Q_i^d \, q_i(\ell+\delta\ell) \tag{36}$$

where $\underline{q}(\ell+\delta\ell)$ is the kinematic parameter obtained by solving the auxiliary problem.
Note that $\left[Q_1^d, \cdots, Q_p^d\right]$ is the set of prescribed static parameters and that when the boundary conditions are only defined by prescribed kinematic parameters $\underline{q}^d$ then $\phi = 0$, this will be the case in the sequel.
In the following section, the validity of this approach will be examined.

5 Numerical applications

The energy approach, developed in this paper, is implemented in the generic finite element library GetFEM [65]. In order to validate this approach, we consider a two-dimensional viscoelastic notched semi-circular geometry of 75 mm in radius with a central notch of depth ℓ under three-point bending: a vertical downward displacement $q^d(t)$ is imposed over a segment on top of the sample (see Fig. 10) For the numerical simulations, the loading and support surfaces are set to 10^{-3} mm and the notch width is assumed to be zero. We assume a plane state of strain and we reason per unit thickness unless explicitly stated otherwise. In this configuration, the crack propagates in an opening mode. The focus of this section is to numerically implement the energy approach introduced in section 4.3 for dealing with crack growth in asphalt mixtures.

5.1 Notched semi-circular beam without crack growth

5.1.1 Numerical computation energy release rate validation

This section is devoted to the comparison between numerical and semi-analytical energy restitution rates under two different loading conditions defined by a prescribed displacement, i.e. a unique kinematic loading parameter $\mathscr{C}(t) = q^d(t)$ so that the static variable Q as well as the residual kinematic variable q^{ϑ} and the overall compliance S^e are here scalar. To simplify the analytical approach, the homogeneous isotropic material is assumed to behave as a non-ageing linear viscoelastic material with a constant Poisson's ratio ($\nu = 0.35$) and we consider the plane strain framework.
Following the same reasoning as the energetic approach in microporoelasticity, it can be shown that the elastic strain energy can be decomposed into a recoverable energy $\mathcal{W}^e$ and a frozen energy $\mathcal{W}^{res}$ (see A

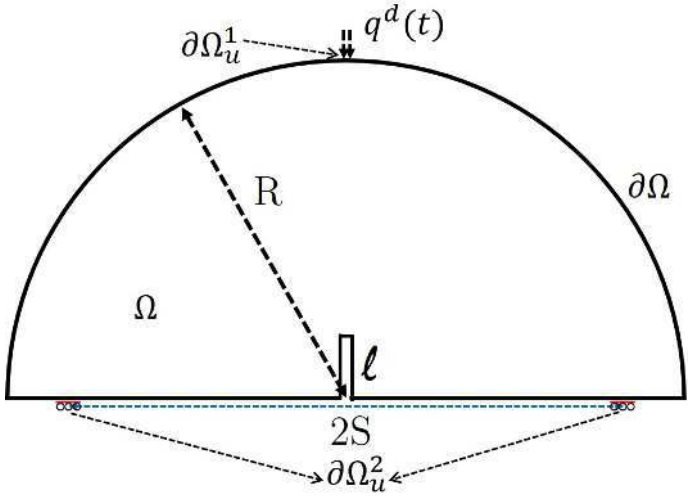

Fig. 10. Semi-circular geometry R= 75 mm, S= 60 mm

for more details):

$$\mathcal{W} = \mathcal{W}^e + \mathcal{W}^{res} \tag{37}$$

where:

$$\mathcal{W}^e = \frac{1}{2}\left(\underline{q} - \underline{q}^\vartheta\right).\underline{\underline{\boldsymbol{S}}}^{e^{-1}}.\left(\underline{q} - \underline{q}^\vartheta\right), \tag{38}$$

$\underline{\underline{\boldsymbol{S}}}^e$ represents the instantaneous global compliance of the system Ω, $\underline{q}$ denotes the global displacement vector and $\underline{q}^\vartheta$ the residual displacement parameter. We have:

$$\underline{q} = \underline{\underline{\boldsymbol{S}}}^e.\underline{Q} + \underline{q}^\vartheta \tag{39}$$

If we consider the alternative form of the elastic strain energy equation (37), the energy release rate equation (32) takes the form:

$$\mathcal{G}_\vartheta(t) = -\frac{1}{2}\frac{\mathrm{d}}{\mathrm{d}\ell}\left(\frac{1}{S^e}\right)\left(q - q^\vartheta\right)^2 + \frac{1}{S^e}\left.\frac{\partial q^\vartheta}{\partial \ell}\right|_{(q^d,\{\underline{\underline{\boldsymbol{\varepsilon}}}_i^\vartheta\})}\left(q - q^\vartheta\right) - \left.\frac{\partial \mathcal{W}^{res}}{\partial \ell}\right|_{(q^d,\{\underline{\underline{\boldsymbol{\varepsilon}}}_i^\vartheta\})} \tag{40}$$

Assuming that the contributions of the derivatives of the residual energy and kinematic parameter are negligible (S. T. Nguyen et al.[68] have rigorously proved this assumption in the case of 1D heterogeneous structures and we propose to verify it in the 3D case), one gets the following reduced form of $\mathcal{G}_\vartheta$:

$$\mathcal{G}_\vartheta(t) \simeq -\frac{1}{2}\frac{\mathrm{d}}{\mathrm{d}\ell}\left(\frac{1}{S^e}\right)\left(q - q^\vartheta\right)^2 \tag{41}$$

Substituting equation (39) into equation (41), this one becomes:

$$\mathcal{G}_\vartheta(t) \simeq \frac{1}{2}\frac{\mathrm{d}S^e}{\mathrm{d}\ell}Q^2 \tag{42}$$

Under the stated assumptions especially constant Poisson's ratio and by application of the principle of superposition, the evolutionary solution defined by the kinematic loading parameter $q^d(t)$ is given by equation (43) [55]:

$$Q(t) = K^e \int_{t_0}^{t} \overline{R}(t-t')\mathrm{d}q^d(t') \tag{43}$$

where $K^e = \dfrac{1}{S^e}$ and $\overline{R}$ is given by equation (7) Substituting equations (43) into the equation (42), the energy release rate thus takes the form:

$$\mathcal{G}_\vartheta(t) \simeq -\frac{1}{2}\frac{\mathrm{d}K^e}{\mathrm{d}\ell}\left(\int_{t_0}^{t} \overline{R}(t-t')\mathrm{d}q^d(t')\right)^2 \tag{44}$$

Let us discuss in more detail the two types of loading envisaged:

- A constant displacement is prescribed $\underline{u}(t) = -U_0\mathcal{H}(t)\underline{e}_y$ ($q^d(t) = U_0\mathcal{H}(t)$ and $\mathcal{H}(t)$ is the Heaviside function). In this case, $\mathcal{G}_\vartheta$ is given by:

$$\mathcal{G}_\vartheta(t) \simeq -\frac{1}{2}\frac{\mathrm{d}K^e}{\mathrm{d}\ell}\left(\overline{R}(t)U_0\right)^2 \tag{45}$$

  The asymptotic energy release rate ($t \to \infty$) yields:

$$\mathcal{G}_\vartheta(t) \underset{t\to\infty}{\longrightarrow} \mathcal{G}_\vartheta^\infty = -\frac{1}{2}\frac{\mathrm{d}K^e}{\mathrm{d}\ell}\left(\frac{E_0U_0}{E^{el}}\right)^2 \tag{46}$$

- A displacement is prescribed in the form $\underline{u}(t) = -\dot{U}t\mathcal{H}(t)\underline{e}_y$ ($q^d(t) = \dot{U}t\mathcal{H}(t)$ and $\dot{U}$ stands for the prescribed constant displacement rate). The energy release rate is expressed as follows:

$$\mathcal{G}_\vartheta(t) \simeq -\frac{1}{2}\frac{\mathrm{d}K^e}{\mathrm{d}\ell}\left(\overline{R}^*(t)\dot{U}t\right)^2 \tag{47}$$

  where $\overline{R}^*$ is given by equation (14) The asymptotic energy release rate ($t \to \infty$) yields:

$$\mathcal{G}_\vartheta(t) \underset{t\to\infty}{\longrightarrow} \mathcal{G}_\vartheta^\infty = \begin{cases} -\dfrac{1}{2}\dfrac{\mathrm{d}K^e}{\mathrm{d}\ell}\left(\dfrac{E_0\dot{U}t}{E^{el}}\right)^2 \longrightarrow \infty & \text{if} \quad E_0 \neq 0 \\ -\dfrac{1}{2}\dfrac{\mathrm{d}K^e}{\mathrm{d}\ell}\left(\dfrac{\dot{U}\sum_{i=1}^{m} E_i\tau_i}{E^{el}}\right)^2 & \text{if} \quad E_0 = 0 \end{cases} \tag{48}$$

It can be shown that $K^e(\ell) = E^{el}K_1^e(\ell)$ where $K_1^e(\ell)$ is the effective stiffness per unit modulus and imposed loading. A numerical determination of $K_1^e(\ell)$ may be easily achieved by standard finite elements. So, the expressions giving $\mathcal{G}_\vartheta$ are semi-analytical in the sense that they are time-based analytical whereas K^e is obtained by solving an elasticity problem using the finite element approach.

The energy release rate can also be defined:

$$\mathcal{G}_1^e(\ell) = -\frac{1}{2}\frac{\mathrm{d}K^e}{\mathrm{d}\ell} \tag{49}$$

Fig. 11 show the effective stiffness and energy release rate calculated for different crack lengths in the semi-circular bending test subjected to a unit displacement and for a unit modulus. The fitted curve

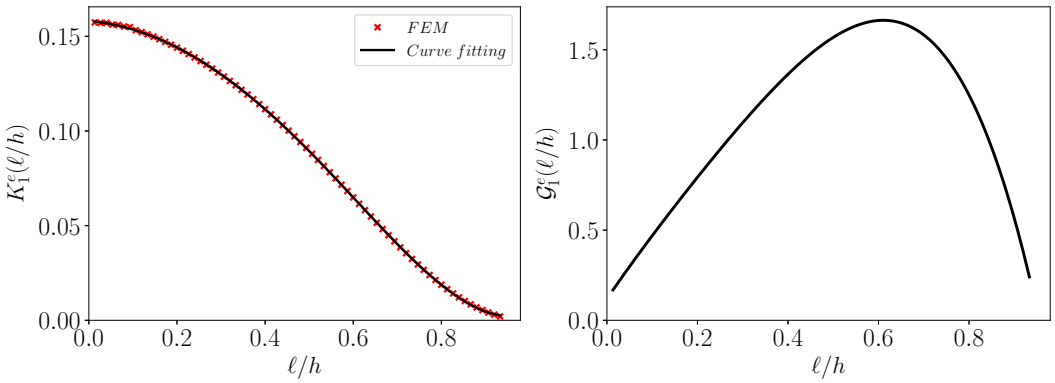

(a) **(b)**

Fig. 11. Effective stiffness and energy release rate calculated for different crack lengths in the SCB test subjected to a unit displacement

equation is given by:

$$K_1^e(x) = 0.209x^5 - 0.18x^4 + 0.11x^3 - 0.275x^2 - 0.018x + 0.158 \quad \text{where } x = \frac{\ell}{R} \tag{50}$$

In order to verify the accuracy of the numerical technique for determining $\mathcal{G}_\vartheta$, numerical resolutions are performed by simulating a semi-circular bending test without crack growth. The viscoelastic properties of the material is given in the Table 2 (material named V0 in the table). The numerical results are compared with our semi-analytical developments (equation (45) and equation (47)). Fig. 12a shows the evolution of the viscoelastic energy release rate over time for a constant imposed displacement and in Fig. 12b, the variation of $\mathcal{G}_\vartheta$ is plotted for a constant imposed displacement rate. A very good agreement between the numerical and semi-analytical solutions can be observed. Under prescribed constant displacement, the decrease of $\mathcal{G}_\vartheta$ as a function of time can also be remarked. This fact reflects the relaxation phenomenon due to the viscoelastic effect. Figures Fig. 13a and Fig. 13b show the asympotic responses of the energy release rate for the two considered loading cases taking $E_0 = 0$.

5.1.2 Progressive or brutal propagation

The notion of stability in the cracking process is very crucial in Griffith's theory [44]. It is proposed here to deal with this question in the viscoelastic framework.

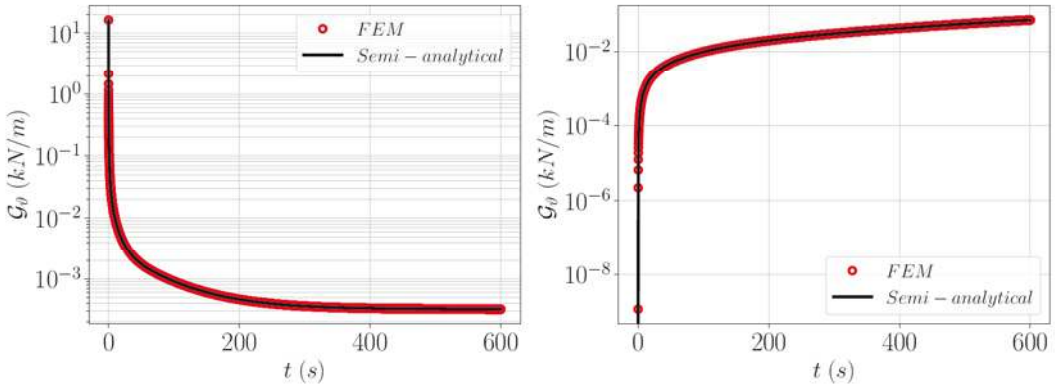

(a) **(b)**

Fig. 12. Evolution of numerical and approximate energy release rates at 20°C without crack growth: Fig. 12a $U_0 = 1$ mm, Fig. 12b $\dot{U} = 1$ mm.min^{-1} ($E_0 = 0$)

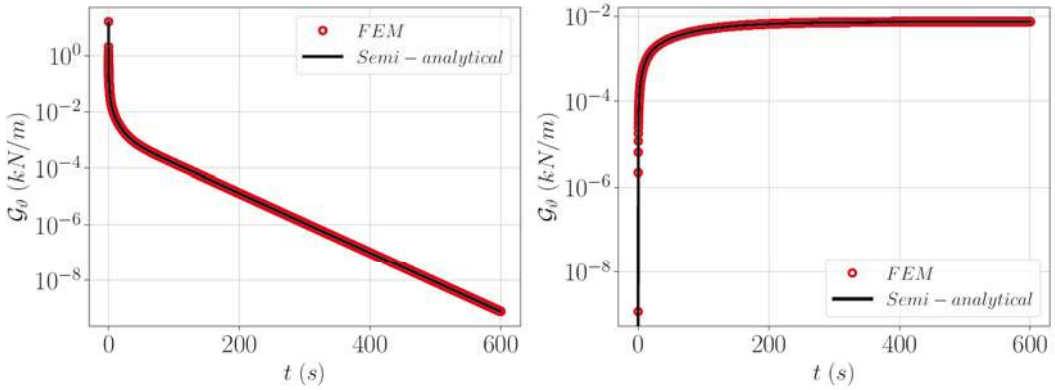

(a) **(b)**

Fig. 13. Evolution of numerical and approximate asymptotic energy release rates at 20°C without crack growth for $E_0 = 0$: Fig. 13a $U_0 = 1$ mm, Fig. 13b $\dot{U} = 1$ mm.min^{-1}

According to Griffith, the stability criterion can be summarised as:

$$\mathcal{G}_\vartheta \leq \mathcal{R} \tag{51}$$

This implies that, at fixed loading and viscous strains, the variation of the ratio between the energy release rate and the crack growth resistance allows to identify the two evolutions of the crack. If this ratio is decreasing with respect to the crack length, then the propagation is stable. To increase cracking, the loading must be increased. However, if this ratio is increasing, then the crack evolution is no longer controlled. If the loading is maintained, the crack will abruptly propagate. In a new state of cracking, under this same loading, the crack may or may not stabilise.

Let's illustrate this by reconsidering the three-point bending test on the semi-circular configuration (see

Fig. 10) subjected to a constant loading rate $\dot{U}$. By assuming that the crack growth resistance is constant ($\mathcal{R} = G_c$) and using relation (47), the ratio $\frac{\mathcal{G}_\vartheta}{\mathcal{R}}$ gives:

$$\frac{\mathcal{G}_\vartheta}{\mathcal{R}} = \mathcal{G}_1^e(\ell) \left(\sqrt{\frac{E^{el}}{G_c}} \overline{R}^*(t)\dot{U}t \right)^2 \tag{52}$$

At a fixed loading, the term $\left(\sqrt{\frac{E^{el}}{G_c}} \overline{R}^*(t)\dot{U}t \right)^2$ being constant, the variation of the ratio $\frac{\mathcal{G}_\vartheta}{\mathcal{R}}$ as a function of ℓ is therefore imposed by $\mathcal{G}_1^e(\ell)$. Under the indicated assumptions, and referring to Fig. 11b, the two situations are distinguished: a phase where the crack propagates abruptly (increasing ratio) followed by a phase of stable propagation (decreasing ratio).

For bituminous mixes, it is well known that the non-linear zone ahead of the crack tip is relatively large compared to the dimensions of the structure and, therefore, its effect cannot be neglected as in linear fracture mechanics. X. Li et al. [69] studied the effect of process fracture zone in bituminous mixtures. They used an eight-channel acoustic emissions system to monitor the fracture process zone during the crack propagation test using an SCB geometry in crack opening mode. They showed that the size of the process zone varies with temperature (the process zone at low temperatures has a greater length than that at high temperatures, while there is no significant difference in width). The authors explain this phenomenon by the viscous behaviour of bituminous mixtures at high temperatures. To take this non-linearity into account, $\mathcal{R}$-curve models have been developed and successfully used to treat cracking problems in wood [70, 71] and concrete [72]. The shape of the $\mathcal{R}$-curve can play a very crucial role in the stability of the crack growth as will be seen in the next section.

5.2 Numerical crack growth algorithm

In order to implement crack growth modelling in finite element software, we present an algorithm which allows finite element coupling between the viscoelastic behaviour and the crack propagation criterion. This paper is limited to the case of a straight crack growth. Thus, the crack path is a priori known. Then we apply the technique known as "unbuttoning nodes" to treat numerically the crack growth of a length $\delta\ell$ when the criterion equation (28) is verified.

In practice, for a virtual crack advance $\delta\ell$, we look for the loading q^d (prescribed displacement for clarity) for which the criterion is fulfilled, i.e. $\mathcal{G}_\vartheta(\ell, q^d) - \mathcal{R} = 0$. The first step is to determine the loading q_c^d that would propagate the crack by a length $\delta\ell$. For a constant loading rate ($\dot{q}^d$), the loading parameter q^d can be written in the incremental form equation (53).

$$q_{n+1}^d = q_n^d + \dot{q}^d \Delta_n t \quad ; \Delta_n t = t_{n+1} - t_n \tag{53}$$

where q_{n+1}^d is determined by looking for the time increment $\Delta_n t$ that ensures a propagation of $\ell + \delta\ell$. Thus for each q_i^d, the energy release rate $\mathcal{G}_\vartheta^i$ is computed. Let us denote by q_k^d, the loading at which

$\mathcal{G}_\vartheta^k > \mathcal{R}$ for the first time. The criterion is then unfulfilled and it becomes necessary to determine the displacement $q_k^{d\,j}$, close to q_k^d such that :

$$f(q_k^{d\,j}) = \mathcal{G}_\vartheta(q_k^{d\,j}) - \mathcal{R} = 0 \tag{54}$$

The equation (54) is resolved using the secant method which provides the following recurrence relation:

$$q_k^{d\,j+1} = q_k^{d\,j} - \frac{q_k^{d\,j} - q_k^{d\,j-1}}{f(q_k^{d\,j}) - f(q_k^{d\,j-1})} f(q_k^{d\,j}) \tag{55}$$

with $q_k^{d\,0} = q_{k-1}$ and $q_k^{d1} = q_k$.

Or:

$$\Delta_k^{j+1}t = \Delta_k^j t - \frac{\Delta_k^j t - \Delta_k^{j-1} t}{f(q_k^{d\,j}) - f(q_k^{d\,j-1})} f(q_k^{d\,j}) \tag{56}$$

with $\Delta_k^0 t = \Delta_{k-1} t$ and $\Delta_k^1 t = \Delta_k t$.

The calculation is interrupted when:

$$|f(q_k^{d\,j})| \leq \varepsilon_\ell \tag{57}$$

where ε_ℓ represents the approximation error committed on the accuracy of the numerical solution. Once the displacement q_c^d is determined (with a tolerance ε_ℓ), the crack is allowed to propagate by a length $\delta\ell$. If the sequence $\left(q_k^{d\,j}\right)$ diverges, which would mean that the reference solution q_k^d is very far from the zero of the function f, then it is necessary to decrease the loading step (and thus the time increment) and restart the calculation. The algorithm for solving the crack growth problem as described above is summarised by the scheme Fig. 14.

6 Comparison between numerical model and experiments

In the framework of numerical simulation, the three-point bending problem is implemented using the finite element library Getfem++ [65] and compared to the experimental results.

6.1 Numerical simulation of the semi-circular bending test

The objective of this section is to evaluate the relevance of the model by comparing the response of the numerical simulations with the experimental observations. The standard crack propagation test on a semi-circular asphalt mixtures specimen is again considered (see Fig. 10). The dimensions used in the simulations are given in section 3.2.2. In order to conduct the 2D numerical simulations of Mode I crack propagation, the following assumptions are adopted:

- Isotropic linear viscoelastic material, homogeneous, whose viscoelastic parameters of the MG model are given in Table 2 for the reference material and for the materials subjected to the 3 and 6 days ageing times.

- Constant Poisson's ratio $\nu = 0.35$

In this study, the formulation of the $\mathcal{R}$ curve developed by Bathias [73, 74] is used:

$$\mathcal{R} = [\alpha + \beta\,(\ell - \ell_0)]^{\frac{1}{\lambda}} \tag{58}$$

where α, β and λ are constants. In the crack growth process, it is shown that the total internal energy, which is equal to the external work done, is composed of the recoverable strain energy, the energy dissipated by the fracture process and the energy dissipated due to the viscoelasticity of the material. The latter term is difficult to identify in the energy analysis balance. The force-displacement method used by Morel et al. [70] cannot be applied to determine the $\mathcal{R}$-curve in viscoelastic media in which the viscous dissipation may not be neglected. For this reason, the $\mathcal{R}$-curve parameters are determined by an optimisation approach. These parameters can be determined by calibrating the peak load and the area under the force-displacement curve between the numerical simulations and the experimental results. The $\mathcal{R}$-values and summarized in Table 3. Figures 15a and 15b illustrate the SCB test simulation results

Table 3: Optimised parameters of the $\mathcal{R}$-curve expression

	$\dot{U}$	α	β	λ
$V0$	1	6.41×10^{-2}	1.43×10^{3}	1.31
	5	8.81×10^{-2}	4.04×10^{3}	1.20
$V3$	1	6.4×10^{-2}	9.49×10^{3}	1.77
	5	6.53×10^{-2}	4.23×10^{3}	1.10
$V6$	1	8.40×10^{-2}	1.44×10^{3}	1.06
	5	6.37×10^{-2}	5.02×10^{3}	1.05

obtained by the finite element method.

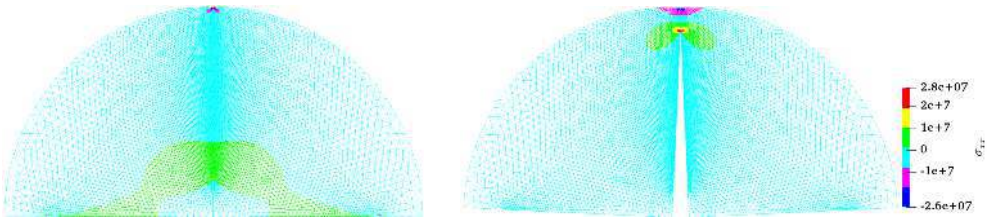

(a) **(b)**

Fig. 15. Crack paths in the numerical simulation for the reference material V0: 15a start of crack growth, 15b end of crack growth

Figures Fig. 16a and Fig. 16b show the numerical variations in crack growth during loading for the two loading rates (1 mm.min^{-1} and 5 mm.min^{-1}) and for the reference material (V0) and the materials conditioned to long-term ageing for 3 and 6 days (V3 and V6).

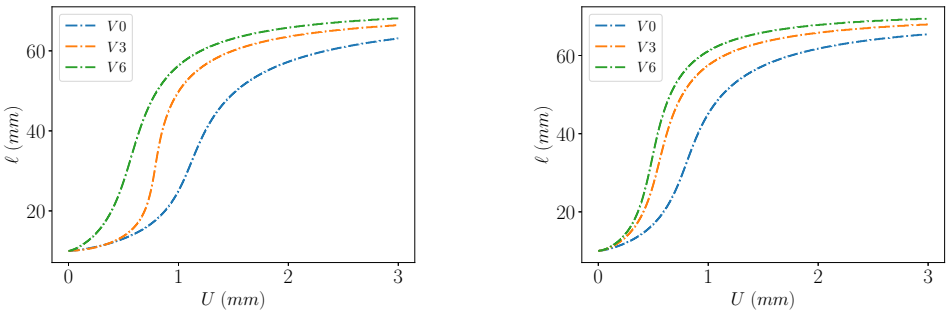

(a) **(b)**

Fig. 16. Evolution of crack length as a function of applied displacement at 0, 3 and 6 day ageing times: 16a for 1 mm.min^{-1} , 16b for 5 mm.min^{-1}

It is noted that as the loading rate increases, the crack propagates more quickly. This result is in agreement with Nguyen et al. conclusions [68]. These figures also show that oxidative ageing leads to an increase in crack growth rate which becomes more pronounced at 5 mm.min^{-1} (see Fig. 16). Figures Fig. 17a and Fig. 17b show the evolution of the $\mathcal{R}$-curve versus the crack length ($\ell - \ell_0$). An increase in R is observed as a function of the loading rate and the ageing time. The reason for this may be that the bituminous mix exhibits less viscous and less ductile behaviour and the development of defects becomes significant with increasing ageing time.

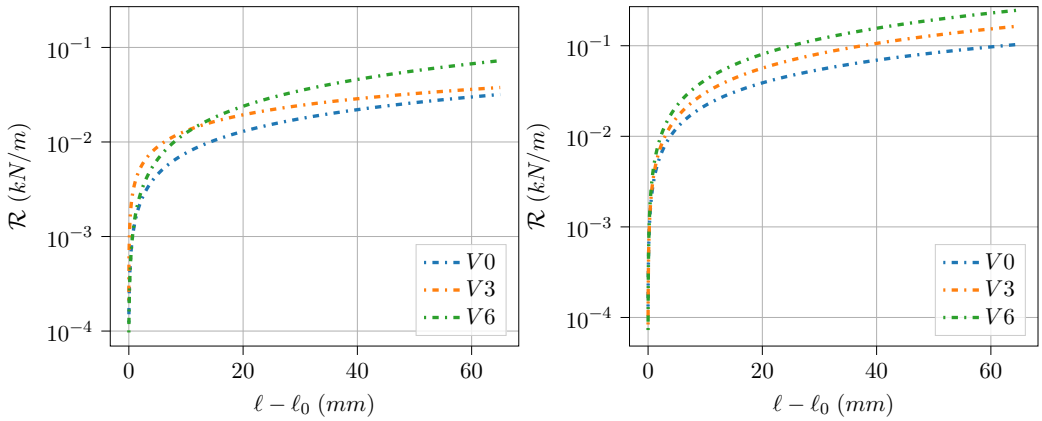

(a) **(b)**

Fig. 17. $\mathcal{R}$-curve evolution as a function of crack length at 0, 3 and 6 day ageing times: 17a for 1 mm.min^{-1} , 17b for 5 mm.min^{-1}

The numerical simulation results, in terms of load-displacement, are validated by comparing them with the experimental results, as shown in Fig. 18a-18f. In a general way, it can be seen that, for each ageing time and loading rate, the numerical and experimental load-displacement curves are consistent for the selected specimens. Nevertheless, we note that the accuracy of the model decreases when the material

is more exposed to ageing and under a higher loading rate. We think that these discrepancies between the numerical simulations and the experimental results may be related to the increase in the size of the process zone (with the ageing duration) limiting its consideration by the $\mathcal{R}$-curve model. An attempt can be made to overcome this problem by using another form of $\mathcal{R}$-curve expression like the one proposed by J. Lemaitre and J-L Chaboche [75] which make the $\mathcal{R}$-expression depend on the crack velocity. Thus, the proposed crack growth criterion, which assumes that the part of the dissipation due to the creation of a crack surface is proportional to the crack velocity, needs to be reconsidered. However, when several specimens are tested, account should be taken of the heterogeneity between specimens which may lead to a dispersion of the test results.

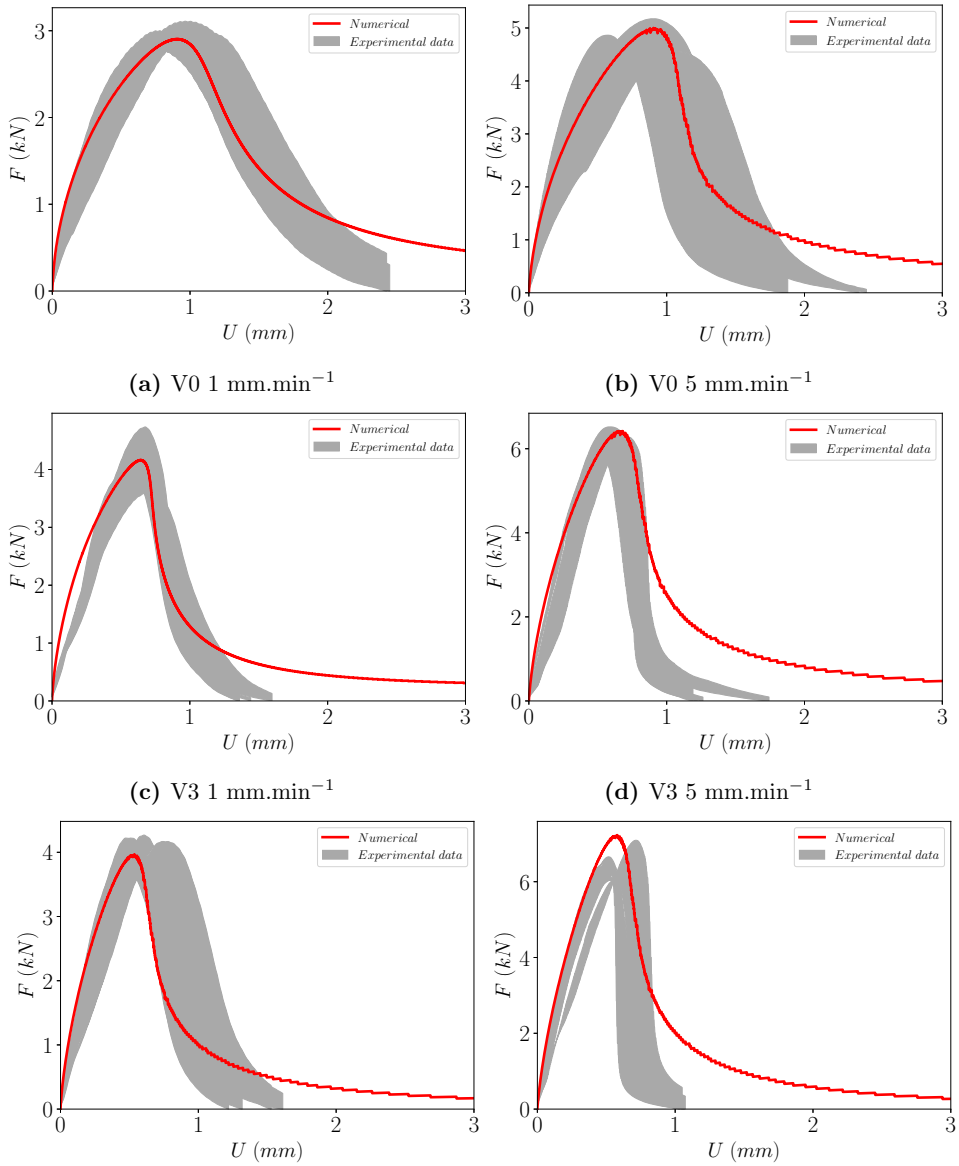

(a) V0 1 mm.min^{-1} **(b)** V0 5 mm.min^{-1}

(c) V3 1 mm.min^{-1} **(d)** V3 5 mm.min^{-1}

(e) V6 1 mm.min^{-1} **(f)** V6 5 mm.min^{-1}

Fig. 18. Comparison of force-displacement curves between numerical and experimental results at 20°C

7 Conclusion

The development of an energetic crack growth model for viscoelastic media is presented in this paper. This model is intended for the study of the fracture of bituminous mixes. For this purpose, the analogue Generalized Maxwell model is used to represent the 3D viscoelastic discretized behaviour of the latter.

This model is implemented in a finite element software GetFem. At the same time, The discretized law is applied to the analysis of a part of the complex modulus tests (2PB-PR) carried out in the laboratory on bituminous mixes at room temperature (20°C) and under 4 loading frequencies ranging from 3 to 40 Hz. A good agreement between the experimental and numerical results has been obtained, which led to the validation of the implemented incremental law. Next, a mechanical model of crack growth in dissipative media has been described. For the first time, analytical expressions of the crack growth driving force as a function of the type of loading is formulated for a semi-circular geometry subjected to three-point bending. This analytical strategy provided a basis for the validation of the numerical determination of the driving force implemented in a Getfem FE software. Finally, the developed model is applied for the very first time to simulate the SCB test performed in the laboratory on bituminous mixtures at 20°C and under two imposed displacement rates (1 mm.min^{-1} and 5 mm.min^{-1}) for the reference and aged mixtures. By dependently setting the $\mathcal{R}$-curve parameters on the loading rate and ageing, a good match between the experimental and numerical results in terms of the force-displacement curve is obtained for all investigated test conditions, thus proving the ability of our model to simulate the ductile crack growth in bituminous mixes under monotonic loading. Taking into account the dependence of the cracking resistance $\mathcal{R}$ on a parameter that is a function of the loading rate (a hardening parameter defined by the residual displacement rates $\underline{\dot{q}}^{\vartheta}$ by analogy with the hardening laws in plasticity) can thus improve the predictive potential of the model and will be investigated in future.

Aiming at refining the model by representing the heterogeneous composition of the herein considered materials, while remaining within reasonable numerical simulation times and further approximating the real material composition (heterogeneity), evolutionary multi-model formulations, articulated within the multi-scale and multi-model Arlequin framework, initiated in [76, 77] and where the overall behaviour can be modelled by homogenisation schemes extended to the viscoelastic medium (e.g. [78, 79]) will be conducted and implemented in the future.

Acknowledgements

The authors would like to thank Arnaud FEESER at Cerema Strasbourg for his kind help in carrying out the semi-circular bending crack propagation tests.

A Decomposition of elastic strain energy

Following the same reasoning as the energetic approach in microporoelasticity (see [68, 80]), the local problem of $(\mathcal{P})$ at fixed crack length $\ell(t)$ with the alternative constitutive law equation (19) can be separated in two loading cases:

1. The first load case we consider is the generalized forces $\underline{\mathscr{C}}$, while pre-strain field $\underline{\underline{\boldsymbol{\varepsilon}}}^{\vartheta}$ is zero:

$$\left(\mathcal{P}^{'}\right): \begin{cases} \mathrm{div}\underline{\underline{\boldsymbol{\sigma}}}' = \underline{0} \quad \text{in } \Omega \\ \underline{\underline{\boldsymbol{\sigma}}}' = \underset{\sim}{\boldsymbol{C}}^{el} : \underline{\underline{\boldsymbol{\varepsilon}}}' \quad \text{in } \Omega \\ \underline{\underline{\boldsymbol{\sigma}}}' \quad \text{is statically admissible with } \underline{\mathrm{Q}} \end{cases} \tag{59}$$

The solution of the evolution problem $\left(\mathcal{P}^{'}\right)$ is given by:

$$\begin{aligned} \underline{\underline{\boldsymbol{\varepsilon}}}' &= \underline{\underline{\underline{\boldsymbol{A}}}}.\underline{Q} \\ \underline{\underline{\boldsymbol{\sigma}}}' &= \underline{\underline{\underline{\boldsymbol{B}}}}.\underline{Q} \\ \underline{q}' &= \underline{\underline{\boldsymbol{S}}}^{e}(\ell) : \underline{Q} \end{aligned} \tag{60}$$

where $\underline{\underline{\underline{\boldsymbol{A}}}}$ and $\underline{\underline{\underline{\boldsymbol{B}}}}$ are respectively third order strain and stress concentration tensors fields. $\underline{\underline{\boldsymbol{S}}}^{e}$ represents the instantaneous global compliance of the system Ω which is symmetric by virtue of the Maxwell-Betti reciprocal theorem.

2. The second load case corresponds to a loading defined by the eigenstrain $\underline{\underline{\boldsymbol{\varepsilon}}}^{\vartheta}$ field (actually defined by all the fields $\underline{\underline{\boldsymbol{\varepsilon}}}^{\vartheta}_{i}$) only:

$$\left(\mathcal{P}^{''}\right): \begin{cases} \mathrm{div}\underline{\underline{\boldsymbol{\sigma}}}'' = \underline{0} \quad \text{in } \Omega \\ \underline{\underline{\boldsymbol{\sigma}}}'' = \underset{\sim}{\boldsymbol{C}}^{el} : \left(\underline{\underline{\boldsymbol{\varepsilon}}}'' - \underline{\underline{\boldsymbol{\varepsilon}}}^{\vartheta}\right) \quad \text{in } \Omega \\ \underline{\underline{\boldsymbol{\sigma}}}'' \quad \text{is statically admissible with } \underline{\mathrm{Q}}=\underline{0} \end{cases} \tag{61}$$

Let us denote by $\underline{q}^{\vartheta}$ the residual displacement parameter, solution of the problem $\left(\mathcal{P}^{''}\right)$. According to the virtual work theorem one has:

$$\begin{aligned} \underline{q}^{\vartheta}.\underline{\hat{Q}} &= \int_{\Omega} \left(\underline{\underline{\boldsymbol{\varepsilon}}}^{\vartheta} + \underset{\sim}{\boldsymbol{C}}^{el^{-1}} : \underline{\underline{\boldsymbol{\sigma}}}''\right) : \underline{\underline{\hat{\boldsymbol{\sigma}}}}\, \mathrm{d}\Omega \\ &= \left(\int_{\Omega} \underline{\underline{\boldsymbol{\varepsilon}}}^{\vartheta} : \underline{\underline{\underline{\boldsymbol{B}}}}\, \mathrm{d}\Omega\right).\underline{\hat{Q}} + \int_{\Omega} \underline{\underline{\boldsymbol{\sigma}}}'' : \underline{\underline{\hat{\boldsymbol{\varepsilon}}}}\, \mathrm{d}\Omega \qquad \forall \underline{\hat{Q}} \\ \underline{q}^{\vartheta}.\underline{\hat{Q}} &= \left(\int_{\Omega} \underline{\underline{\boldsymbol{\varepsilon}}}^{\vartheta} : \underline{\underline{\underline{\boldsymbol{B}}}}\, \mathrm{d}\Omega\right).\underline{\hat{Q}}, \text{ because } \underline{\underline{\boldsymbol{\sigma}}}'' \text{ is self-equilibrating stress} \end{aligned} \tag{62}$$

Therefore we have:

$$\underline{q}^{\vartheta} = \int_{\Omega} \underline{\underline{\boldsymbol{\varepsilon}}}^{\vartheta} : \underline{\underline{\underline{\boldsymbol{B}}}}\, \mathrm{d}\Omega \tag{63}$$

The global vector $\underline{q}$ can then be written:

$$\underline{q} = \underline{\underline{\boldsymbol{S}}}^{e}.\underline{Q} + \underline{q}^{\vartheta} \tag{64}$$

On the other hand, the elastic strain energy can be written as follows:

$$\begin{aligned}
\mathcal{W} &= \sum_{i=0}^{m} \int_{\Omega} \frac{1}{2} \left(\underline{\underline{\boldsymbol{\sigma}}}'_i + \underline{\underline{\boldsymbol{\sigma}}}''_i \right) : \underset{\sim}{\boldsymbol{C}}_i^{-1} : \left(\underline{\underline{\boldsymbol{\sigma}}}'_i + \underline{\underline{\boldsymbol{\sigma}}}''_i \right) \mathrm{d}\Omega \\
&= \sum_{i=0}^{m} \int_{\Omega} \frac{1}{2} \underline{\underline{\boldsymbol{\sigma}}}'_i : \underline{\underline{\boldsymbol{\varepsilon}}}' \, \mathrm{d}\Omega + \sum_{i=0}^{m} \int_{\Omega} \underline{\underline{\boldsymbol{\sigma}}}''_i : \underline{\underline{\boldsymbol{\varepsilon}}}' \, \mathrm{d}\Omega + \sum_{i=0}^{m} \int_{\Omega} \frac{1}{2} \underline{\underline{\boldsymbol{\sigma}}}''_i : \underset{\sim}{\boldsymbol{C}}_i^{-1} : \underline{\underline{\boldsymbol{\sigma}}}''_i \, \mathrm{d}\Omega \\
&= \sum_{i=0}^{m} \int_{\Omega} \frac{1}{2} \underline{\underline{\boldsymbol{\sigma}}}'_i : \underline{\underline{\boldsymbol{\varepsilon}}}' \, \mathrm{d}\Omega + \sum_{i=0}^{m} \int_{\Omega} \frac{1}{2} \underline{\underline{\boldsymbol{\sigma}}}''_i : \underset{\sim}{\boldsymbol{C}}_i^{-1} : \underline{\underline{\boldsymbol{\sigma}}}''_i \, \mathrm{d}\Omega, \text{ because } \underline{\underline{\boldsymbol{\sigma}}}'' \text{ is statically admissible} \\
&\quad \text{with } \underline{Q}=\underline{0} \text{ and } \underline{\underline{\boldsymbol{\varepsilon}}}' \text{ is geometrically compatible} \\
\mathcal{W} &= \mathcal{W}^e + \mathcal{W}^{res}
\end{aligned} \tag{65}$$

where $\mathcal{W}^e$ denotes the recoverable energy and $\mathcal{W}^{res}$ the frozen energy that remains after unloading:

$$\begin{aligned}
\mathcal{W}^e &= \sum_{i=0}^{m} \int_{\Omega} \frac{1}{2} \underline{\underline{\boldsymbol{\sigma}}}'_i : \underline{\underline{\boldsymbol{\varepsilon}}}' \, \mathrm{d}\Omega \\
&= \frac{1}{2} \underline{q}' . \underline{Q} \\
\mathcal{W}^e &= \frac{1}{2} \left(\underline{q} - \underline{q}^{\vartheta} \right) . \underline{\underline{\boldsymbol{S}}}^{e^{-1}} . \left(\underline{q} - \underline{q}^{\vartheta} \right)
\end{aligned} \tag{66}$$

and

$$\begin{aligned}
\mathcal{W}^{res} &= \sum_{i=0}^{m} \int_{\Omega} \frac{1}{2} \underline{\underline{\boldsymbol{\sigma}}}''_i : \underset{\sim}{\boldsymbol{C}}_i^{-1} : \underline{\underline{\boldsymbol{\sigma}}}''_i \, \mathrm{d}\Omega \\
&= \sum_{i=0}^{m} \int_{\Omega} \frac{1}{2} \left(\underline{\underline{\boldsymbol{\varepsilon}}}'' - \underline{\underline{\boldsymbol{\varepsilon}}}_i^{\vartheta} \right) : \underline{\underline{\boldsymbol{\sigma}}}''_i \, \mathrm{d}\Omega \\
\mathcal{W}^{res} &= -\sum_{i=0}^{m} \int_{\Omega} \frac{1}{2} \underline{\underline{\boldsymbol{\varepsilon}}}_i^{\vartheta} : \underline{\underline{\boldsymbol{\sigma}}}''_i \, \mathrm{d}\Omega
\end{aligned} \tag{67}$$

It is well demonstrated by equations (63) and (67) that the residual displacement field $\underline{q}^{\vartheta}$ and the frozen energy $\mathcal{W}^{res}$ both depend on the viscous strains field.

References

[1] Airey G.D. State of the Art Report on Ageing Test Methods for Bituminous Pavement Materials. *International journal of pavement engineering*, 4(3):165–176, 2003.

[2] Bressi S., Carter A., Bueche N., and Dumont A-G. Impact of different ageing levels on binder rheology. *International journal of pavement engineering*, 17(5):403–413, 2016.

[3] Das P. K., Kringos N., and Birgisson B. Numerical study on the effect of mixture morphology on long-term asphalt mixture ageing. *International journal of pavement engineering*, 16(Issue 8):710–720, 2015.

[4] Braham A. F., Buttlar W. G., Clyne T. R., Marasteanu M. O., and Turos M. I. The effect of long-term laboratory aging on asphalt concrete fracture energy. *Journal of the Association of Asphalt Paving Technologists*, 78:417–445, 2009.

[5] Farhad Y. R., Elwardany M. D., Castorena C., and Kim Y. R. Investigation of proper long-term laboratory aging temperature for performance testing of asphalt concrete. *Construction and Building Materials*, 147:616–629, 2017.

[6] B Kouevidjin, J-F Barthélémy, C Somé, H Ben Dhia, and A Feeser. Effect of thermal ageing on the mechanical properties and cracking behaviour of asphalt concrete. In *RILEM International Symposium on Bituminous Materials*, pages 631–637. Springer, 2020.

[7] Lim I. L., Johnston I. W., and Choi S. K. Stress intensity factors for semi-circular specimens under three-point bending. *Engineering Fracture Mechanics*, 44(3):363–382, 1993.

[8] Molenaar J. M. M. *Performance related characterisation of the mechanical behaviour of asphalt mixtures*. doctoral thesis, Civil Engineering and Geosciences, January 2004.

[9] Kuruppu M. D. and Chong K. P. Fracture toughness testing of brittle materials using semi-circular bend (scb) specimen. *Engineering Fracture Mechanics*, 91:133–150, 2012.

[10] Saha G. and Biligiri K. P. Fracture properties of asphalt mixtures using semi-circular bending test: a state-of-the-art review and future research. *Construction and Building Materials*, 105:103–112, 2016.

[11] Somé S. C., Feeser A., and Pavoine A. Numerical and experimental investigation of mode I cracking of asphalt concrete using semi-circular bending test. *Construction and Building Materials*, 169:34–46, 2018.

[12] Somé S. C., Fredj M. A., Nguyen M-L., Feeser A., and Pavoine A. Multi-parametric characterization of mode I fracture toughness of asphalt concrete: Influence of void and RA contents, binder and aggregate types. *International Journal of Pavement Research and Technology*, 11(3):274–284, 2018.

[13] Knauss W. G. Delayed failurethe griffith problem for linearly viscoelastic materials. *International Journal of Fracture Mechanics*, 6(1):7–20, 1970.

[14] Knauss W. G. A review of fracture in viscoelastic materials. *International Journal of Fracture*, 196(1-2):99–146, 2015.

[15] Schapery R. A. A theory of crack initiation and growth in viscoelastic media i. *International Journal of Fracture*, 11(1):141–159, 1975.

[16] Schapery R. A. A theory of crack initiation and growth in viscoelastic media ii. approximate methods of analysis. *International Journal of Fracture*, 11(3):369–388, 1975.

[17] Schapery R. A. Correspondence principles and a generalized j integral for large deformation and fracture analysis of viscoelastic media. *International Journal of Fracture*, 25(3):195–223, 1984.

[18] Graham G. A. C. and Sabin G. C. W. The correspondence principle of linear viscoelasticity for problems that involve time-dependent regions. *International Journal of Engineering Science*, 11(1):123 – 140, 1973.

[19] Schapery R. A. On some path independent integrals and their use in fracture of nonlinear viscoelastic media. In *Non-Linear Fracture*, pages 189–207. Springer, 1990.

[20] Schapery R. A. Characterization of nonlinear, time-dependent polymers and polymeric composites for durability analysis. *Progress in Durability Analysis of Composite Systems*, pages 21–38, 1996.

[21] Dubois F. *Modélisation du comportement mécanique des milieux viscoélastiques fissurés: Application au matériau bois*. PhD thesis, Limoges, 1997.

[22] Dubois F., Chazal C., and Petit C. A finite element analysis of creep-crack growth in viscoelastic media. *Mechanics of Time-Dependent Materials*, 2(3):269–286, 1998.

[23] Chazal C. and Dubois F. A new incremental formulation in the time domain for crack initiation in an orthotropic linearly viscoelastic solid. *Mechanics of Time-Dependent Materials*, 5(3):229–253, 2001.

[24] Dubois F., Chazal C., and Petit C. Viscoelastic crack growth process in wood timbers: an approach by the finite element method for mode I fracture. *International journal of fracture*, 113(4):367–388, 2002.

[25] Dubois F. and Petit C. Modelling of the crack growth initiation in viscoelastic media by the $G\theta_\vartheta$-integral. *Engineering Fracture Mechanics*, 72(18):2821–2836, 2005.

[26] Brincker R. Crack tip parameters for growing cracks in linear viscoelastic materials. 1990.

[27] Paulino G. H., Song S. H., and Buttlar W. G. Cohesive zone modeling of fracture in asphalt concrete. In *Proceedings of the 5th International RILEM Conference–Cracking in Pavements: Mitigation, Risk Assessment, and Preservation*, pages 63–70. Limoges, France, 2004.

[28] Li X. and Marasteanu M. O. Cohesive modeling of fracture in asphalt mixtures at low temperatures. *International Journal of Fracture*, 136(1-4):285–308, 2005.

[29] Song S. H., Paulino G. H., and Buttlar W. G. Simulation of crack propagation in asphalt concrete using an intrinsic cohesive zone model. *Journal of Engineering Mechanics*, 132(11):1215–1223, 2006.

[30] Song S. H., Paulino G. H., and Buttlar W. G. A bilinear cohesive zone model tailored for fracture of asphalt concrete considering viscoelastic bulk material. *Engineering Fracture Mechanics*, 73(18):2829–2848, 2006.

[31] Kim Y-R., Allen D. H., and Little D. N. Computational constitutive model for predicting nonlinear viscoelastic damage and fracture failure of asphalt concrete mixtures. *International Journal of Geomechanics*, 7(2):102–110, 2007.

[32] Song S. H., Wagoner M. P., Paulino G. H., and Buttlar W. G. $\delta 25$ crack opening displacement parameter in cohesive zone models: experiments and simulations in asphalt concrete. *Fatigue & Fracture of Engineering Materials & Structures*, 31(10):850–856, 2008.

[33] Kim H. and Buttlar W. G. Finite element cohesive fracture modeling of airport pavements at low temperatures. *Cold Regions Science and Technology*, 57(2-3):123–130, 2009.

[34] Aragão F. T. S., Kim Y-R., Lee J., and Allen D. H. Micromechanical model for heterogeneous asphalt concrete mixtures subjected to fracture failure. *Journal of Materials in Civil Engineering*, 23(1):30–38, 2011.

[35] Aragão F. T. S. and Kim Y-R. Mode I fracture characterization of bituminous paving mixtures at intermediate service temperatures. *Experimental mechanics*, 52(9):1423–1434, 2012.

[36] Park K. and Paulino G. H. Cohesive zone models: a critical review of traction-separation relationships across fracture surfaces. *Applied Mechanics Reviews*, 64(6), 2011.

[37] Yoon C. and Allen D. H. Damage dependent constitutive behavior and energy release rate for a cohesive zone in a thermoviscoelastic solid. *International Journal of Fracture*, 96(1):55–74, 1999.

[38] Kim Y.R., Teixeira J. E., Kommidi S. R., Little D. N., Aragao F. T., Manrique-Sanchez L., and Souza F. V. Rate-dependent fracture modeling of bituminous media using nonlinear viscoelastic cohesive zone with gaussian damage function. *Computer-Aided Civil and Infrastructure Engineering*, 2021.

669 [39] Rilin Shen, Haim Waisman, and Licheng Guo. Fracture of viscoelastic solids modeled with a modified
670 phase field method. *Computer Methods in Applied Mechanics and Engineering*, 346:862–890, 2019.

671 [40] Franz Dammaß, Marreddy Ambati, and Markus Kästner. A unified phase-field model of fracture in
672 viscoelastic materials. *Continuum Mechanics and Thermodynamics*, 33(4):1907–1929, 2021.

673 [41] Akoeêteê Kouevidjin. *Caractérisation, modélisation et simulation thermo-viscoélastiques de la fis-*
674 *suration des enrobés bitumineux*. Theses, Université Paris-Saclay, May 2021.

675 [42] Bo Yin, Johannes Storm, and Michael Kaliske. Viscoelastic phase-field fracture using the framework
676 of representative crack elements. *International Journal of Fracture*, pages 1–25, 2021.

677 [43] Benjamin Shiferaw, Olivier Chupin, Jean-Michel Piau, and Nicolas Mos. Development of a damage
678 viscoelastic model using the thick level set approach to fracture: 1d modeling and comparison to
679 uniaxial tension stress tests on bituminous specimens. *Engineering Fracture Mechanics*, 257:108026,
680 2021.

681 [44] Griffith A. A. Vi. the phenomena of rupture and flow in solids. *Philosophical transactions of the*
682 *royal society of london. Series A, containing papers of a mathematical or physical character*, 221(582-
683 593):163–198, 1921.

684 [45] Nguyen S. T., Dormieux L., Le Pape Y., and Sanahuja J. Crack propagation in viscoelastic struc-
685 tures: Theoretical and numerical analyses. *Computational Materials Science*, 50(1):83–91, 2010.

686 [46] Nguyen S.T., Jeannin L., Dormieux L., and Renard F. Fracturing of viscoelastic geomaterials and
687 application to sedimentary layered rocks. *Mechanics Research Communications*, 49:50–56, 2013.

688 [47] EN 1426. Bitumen and bituminous binders - determination of needle penetration. *European Standard*,
689 2018.

690 [48] EN 1427. Bitumen and bituminous binders - determination of the softening point - ring and ball
691 method. *European Standard*, 2018.

692 [49] EN 1097-1. Tests for mechanical and physical properties of aggregates - part 1 : determination of
693 the resistance to wear (micro-deval). *European Standard*, 2011.

694 [50] EN 1097-2. Tests for mechanical and physical properties of aggregates - part 2 : methods for the
695 determination of resistance to fragmentation. *European Standard*, 2010.

696 [51] CEN TS 12697-52. Bituminous mixtures - test methods - part 52: Conditioning to address oxidative
697 ageing, 2017.

698 [52] EN 12697-33. Bituminous mixtures - test methods -part 33 : roller, 2019.

699 [53] EN 12697-26. Bituminous mixtures - test methods - part 26 : stiffness. *European Standard*, 2018.

[54] Wiechert E. Gesetze der elastischen nachwirkung für constante temperatur. *Annalen der Physik*, 286(11):546–570, 1893.

[55] Salençon J. *Viscoélasticité pour le calcul des structures*. Editions Ecole Polytechnique, 2009.

[56] Jean Salençon. *Yield Design*. John Wiley & Sons, Inc., Hoboken, NJ USA, 2013.

[57] Christian Huet. Coupled size and boundary-condition effects in viscoelastic heterogeneous and composite bodies. *Mechanics of Materials*, 31(12):787–829, 1999.

[58] Olard F. and Di Benedetto H. General 2s2p1d model and relation between the linear viscoelastic behaviours of bituminous binders and mixes. *Road Materials and Pavement Design*, 4 Issue 2:185–224, 2003.

[59] Van Thang Vu, Olivier Chupin, Jean-Michel Piau, Ferhat Hammoum, and Stephane Bouron. Experimental study and modeling of the behavior of partially saturated asphalt concrete under freezing condition. *Construction and Building Materials*, 163:169–178, 2018.

[60] Bažant Z. P. *Mathematical modeling of creep and shrinkage of concrete*. Wiley, 1988.

[61] Šmilauer V. and Bažant Z. P. Identification of viscoelastic csh behavior in mature cement paste by fft-based homogenization method. *Cement and Concrete Research*, 40(2):197–207, 2010.

[62] Gudmarsson A., Ryden N., Di Benedetto H., and Sauzéat C. Complex modulus and complex poissons ratio from cyclic and dynamic modal testing of asphalt concrete. *Construction and Building Materials*, 88:20–31, 2015.

[63] Allou F., Takarli M., Dubois F., Petit C., and Absi J. Numerical finite element formulation of the 3d linear viscoelastic material model: Complex poisson's ratio of bituminous mixtures. *Archives of Civil and Mechanical Engineering*, 15(4):1138–1148, 2015.

[64] Zienkiewicz O. C., Taylor R. L., Nithiarasu P., and Zhu J. Z. *The finite element method*, volume 3. McGraw-hill London, 1977.

[65] Renard Y. and Poulios K. Getfem: Automated fe modeling of multiphysics problems based on a generic weak form language. *ACM Transactions on Mathematical Software (TOMS)*, 47(1):1–31, 2020.

[66] Geuzaine C. and Remacle J-F. Gmsh: A 3-d finite element mesh generator with built-in pre-and post-processing facilities. *International journal for numerical methods in engineering*, 79(11):1309–1331, 2009.

[67] Ahrens J., Geveci B., and Law C. Paraview: An end-user tool for large data visualization. *The visualization handbook*, 717, 2005.

[68] Nguyen S. T., Dormieux L., Le Pape Y., and Sanahuja J. Crack propagation in viscoelastic structures: Theoretical and numerical analyses. *Computational Materials Science*, 50 (1):83–91, 2010.

[69] Li X. and Marasteanu M. The fracture process zone in asphalt mixture at low temperature. *Engineering Fracture Mechanics*, 77(7):1175–1190, 2010.

[70] Morel S., Bouchaud E., Schmittbuhl J., and Valentin G. R-curve behavior and roughness development of fracture surfaces. *International Journal of Fracture*, 114(4):307–325, 2002.

[71] Phan N. A. *Simulation of time-dependent crack propagation in a quasi-brittle material under relative humidity variations based on cohesive zone approach : application to wood*. Theses, Université de Bordeaux, January 2016.

[72] Cecot C. *Etude micromcanique par simulation numrique en lments finis des couplages viscolasticit-croissance des fissures dans les composites granulaires de type bton*. PhD thesis, Lausanne, EPFL, 2001.

[73] BATHIAS C. Résistance à la rupture - courbe R. pages 147–173, 1980.

[74] Recho N. *Fracture mechanics and crack growth*. John Wiley & Sons, 2012.

[75] Jean Lemaitre and Jean-Louis Chaboche. *Mechanics of solid materials*. Cambridge university press, 1994.

[76] Hachmi Ben Dhia. Multiscale mechanical problems: the arlequin method. *Comptes Rendus de l'Academie des Sciences Series IIB Mechanics Physics Astronomy*, 12(326):899–904, 1998.

[77] H Ben Dhia. Analyse mathématique de la méthode arlequin mixtemathematical analysis of the mixed arlequin method. *Academie des Sciences Paris Comptes Rendus Serie Sciences Mathematiques*, 332(7):649–654, 2001.

[78] J-F Barthélémy, Albert Giraud, J Sanahuja, and I Sevostianov. Effective properties of ageing linear viscoelastic media with spheroidal inhomogeneities. *International Journal of Engineering Science*, 144:103104, 2019.

[79] F Lavergne and J-F Barthélémy. Confronting a refined multiscale estimate for the aging basic creep of concrete with a comprehensive experimental database. *Cement and Concrete Research*, 136:106163, 2020.

[80] Dormieux L., Kondo D., and Ulm F-J. *Microporomechanics*. John Wiley & Sons, 2006.

Highlights

- The viscoelastic crack growth criterion is reviewed and extended to the behaviour of bituminous mixtures.
- A new analytical expression of the energy release rate is presented and applied in detail to the semi-circular bending configuration.
- Numerical simulations of the semi-circular bending test are performed.
- Comparison between numerical and experimental results is analyzed using a new approach combining the proposed model and the R-curve model.

This study is not subject to any conflict of interest.